

# <sup>1</sup> DeepPoseKit, a software toolkit for <sup>2</sup> fast and robust animal pose <sup>3</sup> estimation using deep learning

<sup>4</sup> **Jacob M. Graving<sup>1,2,3,\*</sup>, Daniel Chae<sup>4</sup>, Hemal Naik<sup>1,2,3,5</sup>, Liang Li<sup>1,2,3</sup>, Benjamin**

<sup>5</sup> Koger<sup>1,2,3</sup>, Blair R. Costelloe<sup>1,2,3</sup>, Iain D. Couzin<sup>1,2,3,\*</sup>

\*For correspondence:

jgraving@gmail.com; icouzin@ab.mpg.de

<sup>6</sup> <sup>1</sup>Department of Collective Behaviour, Max Planck Institute of Animal Behavior, 78464 Konstanz, Germany; <sup>2</sup>Department of Biology, University of Konstanz, 78464 Konstanz, Germany; <sup>3</sup>Centre for the Advanced Study of Collective Behaviour, University of Konstanz, 78464 Konstanz, Germany; <sup>4</sup>Department of Computer Science, Princeton University, 08544 Princeton, NJ, USA; <sup>5</sup>Chair for Computer Aided Medical Procedures, Technische Universität München, 80333 Munich, Germany

**Abstract** Quantitative behavioral measurements are important for answering questions across scientific disciplines—from neuroscience to ecology. State-of-the-art deep-learning methods offer major advances in data quality and detail by allowing researchers to automatically estimate locations of an animal’s body parts directly from images or videos. However, currently-available animal pose estimation methods have limitations in speed and robustness. Here we introduce a new easy-to-use software toolkit, *DeepPoseKit*, that addresses these problems using an efficient multi-scale deep-learning model, called *Stacked DenseNet*, and a fast GPU-based peak-detection algorithm for estimating keypoint locations with subpixel precision. These advances improve processing speed >2x with no loss in accuracy compared to currently-available methods. We demonstrate the versatility of our methods with multiple challenging animal pose estimation tasks in laboratory and field settings—including groups of interacting individuals. Our work reduces barriers to using advanced tools for measuring behavior and has broad applicability across the behavioral sciences.

## **Introduction**

Understanding the relationships between individual behavior, brain activity (reviewed by *Krakauer et al. 2017*), and collective and social behaviors (*Rosenthal et al., 2015; Strandburg-Peshkin et al., 2013; Jolles et al., 2017; Klibaite et al., 2017; Klibaite and Shaevitz, 2019*) is a central goal of the behavioral sciences—a field that spans disciplines from neuroscience to psychology, ecology, and genetics. Measuring and modelling behavior is key to understanding these multiple scales of complexity, and, with this goal in mind, researchers in the behavioral sciences have begun to integrate theory and methods from physics, computer science, and mathematics (*Anderson and Perona, 2014; Berman, 2018; Brown and De Bivort, 2018*). A cornerstone of this interdisciplinary revolution is the use of state-of-the-art computational tools, such as computer vision algorithms, to automatically measure locomotion and body posture (*Dell et al., 2014*). Such a rich description of animal movement then allows for modeling, from first principles, the full behavioral repertoire of animals (*Stephens et al., 2011; Berman et al., 2014a, 2016; Wiltschko et al., 2015; Johnson et al., 2016b; Todd et al., 2017; Klibaite et al., 2017; Markowitz et al., 2018; Klibaite and Shaevitz, 2019; Costa et al., 2019*). Tools for automatically measuring animal movement represent a vital first step toward developing unified theories of behavior across scales (*Berman, 2018; Brown and De Bivort, 2018*). Therefore, technical factors like scalability, robustness, and usability are issues of critical importance, especially as researchers across disciplines begin to increasingly rely on these methods.

Two of the latest contributions to the growing toolbox for quantitative behavioral analysis are from *Mathis et al. (2018)* and *Pereira et al. (2019)*, who make use of a popular type of machine learning model called convolutional neural networks, or CNNs (*LeCun et al. 2015*; Appendix 2), to automatically measure detailed representations of animal posture—structural keypoints, or joints, on the animal’s body—directly from images

46 and without markers. While these methods offer a major advance over conventional methods with regard  
47 to data quality and detail, they have disadvantages in terms of speed and robustness, which may limit their  
48 practical applications. To address these problems, we introduce a new software toolkit, called *DeepPoseKit*, with  
49 methods that are fast, robust, and easy-to-use. We run experiments using multiple datasets to compare our new  
50 methods with those from *Mathis et al. (2018)* and *Pereira et al. (2019)*, and we find that our approach offers  
51 considerable improvements. These results also demonstrate the flexibility of our toolkit for both laboratory and  
52 field situations and exemplify the wide applicability of our methods across a range of species and experimental  
53 conditions.

#### 54 **Measuring animal movement with computer vision**

55 Collecting high-quality behavioral data is a challenging task, and while direct observations are important for  
56 gathering qualitative data about a study system, a variety of automated methods for quantifying movement have  
57 become popular in recent years (*Dell et al., 2014; Anderson and Perona, 2014; Kays et al., 2015*). Methods like  
58 video monitoring and recording help to accelerate data collection and reduce the effects of human intervention,  
59 but the task of manually scoring videos is time consuming and suffers from the same limitations as direct  
60 observation, namely observer bias and mental fatigue. Additionally, due to limitations of human observers'  
61 ability to process information, many studies that rely on manual scoring use relatively small datasets to estimate  
62 experimental effects, which can lead to increased rates of statistical errors. Studies that lack the statistical  
63 resolution to robustly test hypotheses (commonly called "power" in frequentist statistics) also raise concerns  
64 about the use of animals for research, as statistical errors caused by sparse data can impact researchers' ability  
65 to accurately answer scientific questions. These limitations have led to the development of automated methods  
66 for quantifying behavior using advanced imaging technologies (*Dell et al., 2014*) as well as sophisticated tags and  
67 collars with GPS, accelerometry, and acoustic-recording capabilities (*Kays et al., 2015*). Tools for automatically  
68 measuring the behavior of individuals now play a central role in our ability to study the neurobiology and  
69 ecology of animals, and reliance on these technologies for studying animal behavior will only increase in the  
70 future.

71 The rapid development of computer vision hardware and software in recent years has allowed for the use of  
72 automated image-based methods for measuring behavior across many experimental contexts (*Dell et al., 2014*).  
73 Early methods for quantifying movement with these techniques required highly-controlled laboratory conditions.  
74 However, because animals exhibit different behaviors depending on their surroundings (*Strandburg-Peshkin*  
75 *et al., 2017; Francisco et al., 2019; Akhund-Zade et al., 2019*), laboratory environments are often less than ideal  
76 for studying many natural behaviors. Most conventional computer vision methods are also limited in their  
77 ability to accurately track groups of individuals over time, but nearly all animals are social at some point in  
78 their life and exhibit specialized behaviors when in the presence of conspecifics (*Strandburg-Peshkin et al.,*  
79 *2013; Rosenthal et al., 2015; Jolles et al., 2017; Klibaite et al., 2017; Klibaite and Shaevitz, 2019; Francisco*  
80 *et al., 2019; Versace et al., 2019*). These methods also commonly track only the animal's center of mass, which  
81 reduces the behavioral output of an individual to a two-dimensional or three-dimensional particle-like trajectory.  
82 While trajectory data are useful for many experimental designs, the behavioral repertoire of an animal cannot  
83 be fully described by its aggregate locomotory output. For example, stationary behaviors, like grooming and  
84 antennae movements, or subtle differences in walking gaits cannot be reliably detected by simply tracking an  
85 animal's center of mass (*Berman et al., 2014a; Wiltschko et al., 2015*).

86 Together these factors have driven the development of software that can accurately track the positions of  
87 marked (*Crall et al., 2015; Graving, 2017; Wild et al., 2018; Boenisch et al., 2018*) or unmarked (*Pérez-Escudero*  
88 *et al., 2014; Romero-Ferrero et al., 2019*) individuals as well as methods that can quantify detailed descriptions  
89 of an animal's posture over time (*Stephens et al., 2011; Berman et al., 2014a; Wiltschko et al., 2015; Mathis*  
90 *et al., 2018; Pereira et al., 2019*). Recently these advancements have been further improved through the  
91 use of deep learning, a class of machine learning algorithms that learn complex statistical relationships from  
92 data (*LeCun et al., 2015*). Deep learning has opened the door to accurately tracking large groups of marked  
93 (*Wild et al., 2018; Boenisch et al., 2018*) or unmarked (*Romero-Ferrero et al., 2019*) individuals and has made  
94 it possible to measure the body posture of animals in nearly any context—including in the wild (*Nath et al.,*  
95 *2019*)—by tracking the positions of user-defined body parts (*Mathis et al., 2018; Pereira et al., 2019*). These  
96 advances have drastically increased the quality and quantity, as well as the diversity, of behavioral data that are  
97 potentially available to researchers for answering scientific questions.

#### 98 **Animal pose estimation using deep learning**

99 In the past, conventional methods for measuring posture with computer vision relied on species-specific algo-  
100 rithms (*Uhlmann et al., 2017*), highly-specialized or restrictive experimental setups (*Mendes et al., 2013; Kain*  
101 *et al., 2013*), attaching intrusive physical markers to the study animal (*Kain et al., 2013*), or some combination

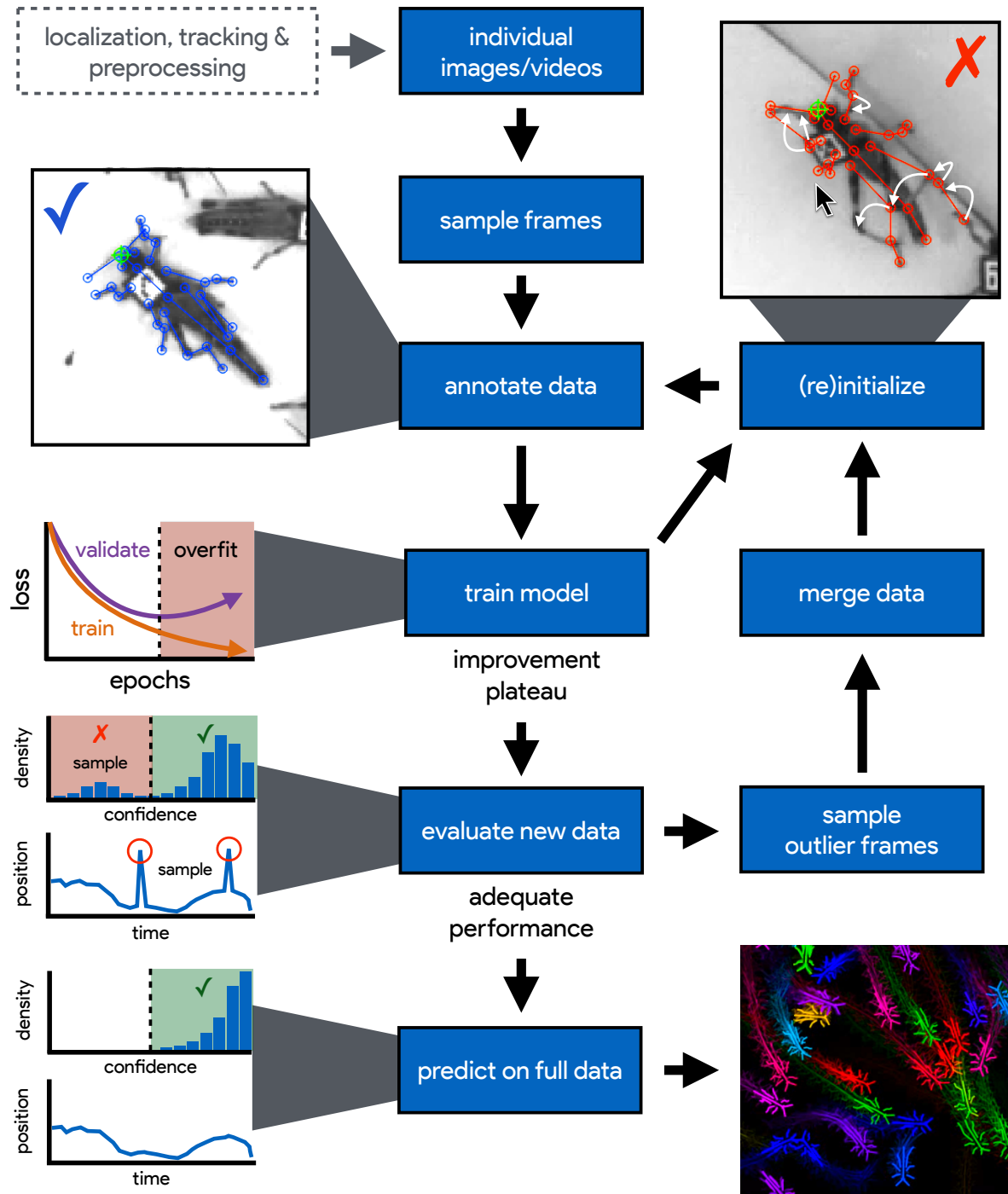


**Figure 1.** An illustration of the workflow for DeepPoseKit. Multi-individual images are localized, tracked, and preprocessed into individual images, which is not required for single-individual image datasets. An initial image set is sampled, annotated, and then iteratively updated using the active learning approach described by Pereira *et al.* (2019) (see Appendix 3). As annotations are made, the model is trained (Figure 2) with the current training set and keypoint locations are initialized for unannotated data to reduce the difficulty of further annotations. This is repeated until there is a noticeable improvement plateau for the initialized data—where the annotator is providing only minor corrections—and for the validation error when training the model (Appendix 1 Figure 4). New data from the full dataset are evaluated with the model, and the training set is merged with new examples that are sampled based on the model's predictive performance, which can be assessed with techniques described by Mathis *et al.* (2018); Nath *et al.* (2019) for identifying outlier frames and minimizing extreme prediction errors—shown here as the distribution of confidence scores predicted by the model and predicted body part positions with large temporal derivatives—indicating extreme errors. This process is repeated as necessary until performance is adequate when evaluating new data. The pose estimation model can then be used to make predictions for the full data set, and the data can be used for further analysis.

**Figure 1-video 1.** A visualization of the posture data output for a group of locusts (5x speed) <https://youtu.be/hCa2zaoUWhs>.

102 thereof. These methods also typically required expert computer-vision knowledge to use, were limited in the  
103 number or type of body parts that could be tracked (*Mendes et al., 2013*), involved capturing and handling  
104 the study animals to attach markers (*Kain et al., 2013*)—which is not possible for many species—and despite  
105 best efforts to minimize human involvement, often required manual intervention to correct errors (*Uhlmann  
106 et al., 2017*). All of these methods were built to work for a small range of conditions and typically required  
107 considerable effort to adapt to novel contexts.

108 In contrast to conventional computer-vision methods, modern deep-learning-based methods can be used  
109 to achieve near human-level accuracy in almost any scenario by manually annotating data (Figure 1)—known as  
110 a *training set*—and training a general-purpose image-processing algorithm—a convolutional neural network or  
111 CNN—to automatically estimate the locations of an animal’s body parts directly from images (Figure 2). State-of-  
112 the-art machine learning methods, like CNNs, use these training data to parameterize a model describing the  
113 statistical relationships between a set of input data—i.e., images—and the desired output distribution—i.e.,  
114 posture keypoints. After adequate training, a model can be used to make predictions on previously-unseen  
115 data from the same dataset—inputs that were not part of the training set, which is known as *inference*. In other  
116 words, these models are able to generalize human-level expertise at scale after having been trained on only a  
117 relatively small number of examples. We provide more detailed background information on using CNNs for  
118 pose estimation in Appendices 2–6.

119 Similar to conventional pose estimation methods, the task of implementing deep-learning models in software  
120 and training them on new data is complex and requires expert knowledge. However, in most cases, once the  
121 underlying model and training routine are implemented, a high-accuracy pose estimation model for a novel  
122 context can be built with minimal modification—often just by changing the training data. With a simplified  
123 toolkit and high-level software interface designed by an expert, even scientists with limited computer-vision  
124 knowledge can begin to apply these methods to their research. Once the barriers for implementing and training  
125 a model are sufficiently reduced, the main bottleneck for using these methods becomes collecting an adequate  
126 training set—a labor-intensive task made less time-consuming by techniques described in Appendix 3.

127 *Mathis et al. (2018)* and *Pereira et al. (2019)* were the first to popularize the use of CNNs for animal pose  
128 estimation. These researchers built on work from the human pose estimation literature (e.g., *Andriluka et al.  
129 2014; Insafutdinov et al. 2016; Newell et al. 2016*) using a type of *fully-convolutional neural network* or *F-CNN*  
130 (*Long et al. 2015*; Appendix 4) often referred to as an *encoder-decoder* model (Appendix 4 Box 1). These models  
131 are used to measure animal posture by training the network to transform images into probabilistic estimates  
132 of keypoint locations, known as *confidence maps* (shown in Figure 2), that describe the body posture for one  
133 or more individuals. These confidence maps are processed to produce the 2-D spatial coordinates of each  
134 keypoint, which can then be used for further analysis.

135 While deep-learning models typically need large amounts of training data, both *Mathis et al. (2018)* and  
136 *Pereira et al. (2019)* have demonstrated that near human-level accuracy can be achieved with few training  
137 examples (Appendix 3). In order to ensure generalization to large datasets, both groups of researchers  
138 introduced ideas related to iteratively refining the training set used for model fitting (*Mathis et al., 2018; Pereira  
139 et al., 2019*). In particular, *Pereira et al. (2019)* describe a technique known as *active learning* where a trained  
140 model is used to initialize new training data and reduce annotation time (Appendix 3). *Mathis et al. (2018)*  
141 describe multiple techniques that can be used to further refine training data and minimize errors when making  
142 predictions on the full dataset. Simple methods to accomplish this include filtering data or selecting new training  
143 examples based on confidence scores or the entropy of the confidence maps from the model output. *Nath et al.  
144 (2019)* also introduced the use temporal derivatives (i.e., speed and acceleration) and autoregressive models to  
145 identify outlier frames, which can then be labeled to refine the training set or excluded from further analysis on  
146 the final dataset (Figure 1).

## 147 Pose estimation models and the speed-accuracy trade-off

148 *Mathis et al. (2018)* developed their pose estimation model, which they call *DeepLabCut*, by modifying a  
149 previously-published model called *DeeperCut* (*Insafutdinov et al., 2016*). The DeepLabCut model (*Mathis et al.,  
150 2018*), like the DeeperCut model, is built on the popular *ResNet* architecture (*He et al., 2016*)—a state-of-the-art  
151 deep-learning model used for image classification. This choice is advantageous because the use of a popular  
152 architecture allows for incorporating a pre-trained encoder to improve performance and reduce the number of  
153 required training examples (*Mathis et al., 2018*), known as *transfer learning* (*Pratt 1993*; Appendix 3)—although,  
154 as will be seen, transfer learning appears to offer little improvement over a randomly-initialized model. However,  
155 this choice of a pre-trained architecture is also disadvantageous as the model is *overparameterized* with >25  
156 million parameters. Overparameterization allows the model to make accurate predictions, but this may come  
157 with the cost of slow inference. To alleviate these effects, work from *Mathis and Warren (2018)* showed that  
158 inference speed for the DeepLabCut model (*Mathis et al., 2018*) can be improved by decreasing the resolution

159 of input images, but this is achieved at the expense of accuracy.

160 With regard to model design, *Pereira et al. (2019)* implement a modified version of a model called *SegNet*  
161 (*Badrinarayanan et al., 2015*), which they call *LEAP* (LEAP Estimates Animal Pose), that attempts to limit model  
162 complexity and overparameterization with the goal of maximizing inference speed (see Appendix 6)—however,  
163 our comparisons from this paper suggest *Pereira et al. (2019)* achieved only limited success compared to the  
164 DeepLabCut model (*Mathis et al., 2018*). The LEAP model is advantageous because it is explicitly designed for  
165 fast inference but has disadvantages such as a lack of robustness to data variance, like rotations or shifts in  
166 lighting, and an inability to generalize to new experimental setups. Additionally, to achieve maximum perfor-  
167 mance, the training routine for the LEAP model introduced by *Pereira et al. (2019)* requires computationally  
168 expensive preprocessing that is not practical for many datasets, which makes it unsuitable for a wide range of  
169 experiments (see Appendix 6 for more details).

170 Together the methods from *Mathis et al. (2018)* and *Pereira et al. (2019)* represent the two extremes of a  
171 phenomenon known as the *speed-accuracy trade-off* (*Huang et al., 2017b*)—an active area of research in the  
172 machine learning literature. *Mathis et al. (2018)* prioritize accuracy over speed by using a large overparam-  
173 eterized model (*Insafutdinov et al., 2016*), and *Pereira et al. (2019)* prioritize speed over accuracy by using a  
174 smaller less-robust model. While this speed-accuracy trade-off can limit the capabilities of CNNs, there has been  
175 extensive work to make these models more efficient without impacting accuracy (e.g., *Chollet 2017; Huang et al.*  
176 *2017a; Sandler et al. 2018*). To address the limitations of this trade-off, we apply recent developments from the  
177 machine learning literature and provide an effective solution to the problem.

178 In the case of F-CNN models used for pose estimation, improvements in efficiency and robustness have  
179 been made through the use of *multi-scale inference* (Appendix 4 Box 1) by increasing connectivity between the  
180 model’s many layers across multiple spatial scales (Appendix 4 Figure 1). Multi-scale inference implicitly allows  
181 the model to simultaneously integrate large-scale global information, such as the lighting, image background,  
182 or the orientation of the focal individual’s body trunk; information from intermediate scales like anatomical  
183 geometry related to cephalization and bilateral symmetry; and fine-scale local information that could include  
184 differences in color, texture, or skin patterning for specific body parts. This multi-scale design gives the model  
185 capacity to learn the hierarchical relationships between different spatial scales and efficiently aggregate them  
186 into a joint representation when solving the posture estimation task (see Box 1 and Appendix 4 Figure 1 for  
187 further discussion)

### 188 **Individual vs. multiple pose estimation**

189 Most work on human pose estimation now focuses on estimating the pose of multiple individuals in an image  
190 (e.g., *Cao et al. 2017*). For animal pose estimation, the methods from *Pereira et al. (2019)* are limited to  
191 estimating posture for single individuals—known as *individual pose estimation*—while the methods from *Mathis*  
192 *et al. (2018)* can also be extended to estimate posture for multiple individuals simultaneously—known as  
193 *multiple pose estimation*. However, the majority of work on multiple pose estimation, including *Mathis et al.*  
194 *(2018)*, has not adequately solved the tracking problem of linking individual posture data across frames in a video,  
195 especially after visual occlusions, which are common in many behavioral experiments—although recent work has  
196 attempted to address this problem (*Iqbal et al., 2017; Andriluka et al., 2018*). Additionally, as the name suggests,  
197 the task of multiple pose estimation requires exhaustively annotating images of multiple individuals—where  
198 every individual in the image must be annotated to prevent the model from learning conflicting information.  
199 This type of annotation task is even more laborious and time consuming than annotations for individual pose  
200 estimation and the amount of labor increases proportionally with the number of individuals in each frame,  
201 which makes this approach intractable for many experimental systems.

202 Reliably tracking the position of individuals over time is important for most behavioral studies, and there  
203 are a number of diverse methods already available for solving this problem (*Pérez-Escudero et al., 2014; Crall*  
204 *et al., 2015; Graving, 2017; Romero-Ferrero et al., 2019; Wild et al., 2018; Boenisch et al., 2018*). Therefore, to  
205 avoid solving an already-solved problem of tracking individuals and to circumvent the cognitively complex task  
206 of annotating data for multiple pose estimation, the work we describe in this paper is purposefully limited to  
207 individual pose estimation—where each image contains only a single focal individual, which may be cropped  
208 from a larger multi-individual image after localization and tracking. We introduce a top-down posture estimation  
209 framework that can be readily adapted to existing behavioral analysis workflows, which could include any  
210 method for localizing and tracking individuals.

211 The additional step of localizing and tracking individuals naturally increases the processing time for producing  
212 posture data from raw image data, which varies depending on the algorithms being used and the number of  
213 individuals in each frame. While tracking and localization may not be practical for all experimental systems,  
214 which could make our methods difficult to apply "out-of-the-box", the increased processing time from automated  
215 tracking algorithms is a reasonable trade-off for most systems given the costly alternative of increased manual

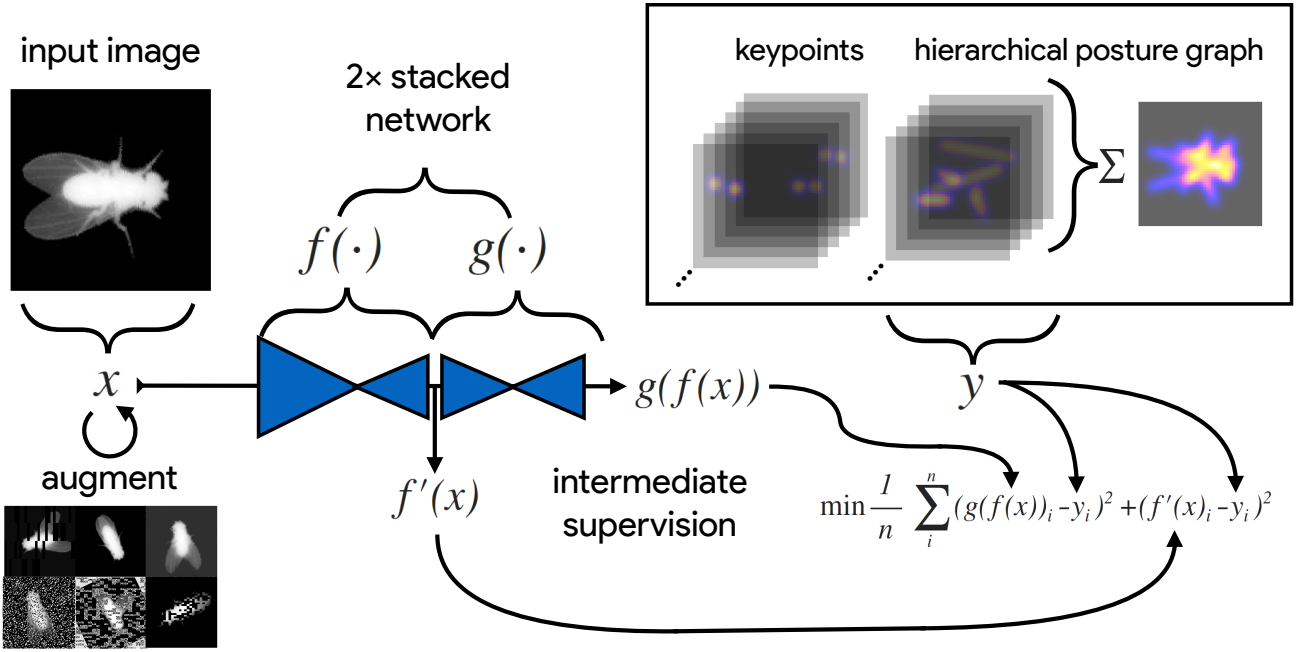


**Figure 2.** An illustration of the model training process for our Stacked DenseNet model in DeepPoseKit (see Appendix 2 for details about training models). Input images  $x$  (**top-left**) are augmented (**bottom-left**) with various spatial transformations (rotation, translation, scale, etc.) followed by noise transformations (dropout, additive noise, blurring, contrast, etc.) to improve the robustness and generalization of the model. The ground truth annotations are then transformed with matching spatial augmentations (not shown for the sake of clarity) and used to draw the confidence maps  $y$  for the keypoints and hierarchical posture graph (**top-right**). The images  $x$  are then passed through the network to produce a multidimensional array  $g(f(x))$ —a stack of images corresponding to the keypoint and posture graph confidence maps for the ground truth  $y$ . Mean squared error between the outputs for both networks  $g(f(x))$  and  $f'(x)$  and the ground truth data  $y$  is then minimized (**bottom-right**), where  $f'(x)$  indicates a subset of the output from  $f(x)$ —only those feature maps being optimized to reproduce the confidence maps for the purpose of intermediate supervision (Appendix 5). The loss function is minimized until the validation loss stops improving—indicating that the model has converged or is starting to overfit to the training data.

216 labor when annotating data. This trade-off seems especially practical when considering that the posture data  
 217 produced by most multiple pose estimation algorithms still need to be linked across video frames to maintain  
 218 the identity of each individual, which is effectively a bottom-up method for achieving the same result. Limiting  
 219 our methods to individual pose estimation also simplifies the pose detection problem as processing confidence  
 220 maps produced by the model does not require computationally-expensive local peak detection and complex  
 221 methods for grouping keypoints into individual posture graphs (e.g., *Insafutdinov et al. 2016; Cao et al. 2017*;  
 222 Appendix 4). Additionally, because individual pose estimation is such a well-studied problem in computer vision,  
 223 we can readily build on state-of-the-art methods for this task (see Appendices 4 and 5 for details).

## 224 Results

225 Here we introduce fast, flexible, and robust pose estimation methods, with a software interface—a high-level  
 226 programming interface (API) and graphical user-interface (GUI) for annotations—that emphasizes usability.  
 227 Our methods build on the state-of-the-art for individual pose estimation (*Newell et al. 2016*; Appendix 5),  
 228 convolutional regression models (*Jégou et al. 2017*; Appendix 4 Box 1), and conventional computer vision  
 229 algorithms (*Guizar-Sicairos et al., 2008*) to improve model efficiency and achieve faster, more accurate results  
 230 on multiple challenging pose estimation tasks. We developed two model implementations—including a new  
 231 model architecture that we call *Stacked DenseNet*—and a new method for processing confidence maps called  
 232 *subpixel maxima* that provides fast and accurate peak detection for estimating keypoint locations with subpixel  
 233 precision—even at low spatial resolutions. We also discuss a modification to incorporate a hierarchical posture  
 234 graph for learning the multi-scale geometry between keypoints on the animal’s body, which increases accuracy  
 235 when training pose estimation models. We ran experiments to optimize our approach and compared our new  
 236 models to the models from *Mathis et al. (2018)* (DeepLabCut) and *Pereira et al. (2019)* (LEAP) in terms of speed,  
 237 accuracy, training time, and generalization ability. We benchmarked these models using three image datasets  
 238 recorded in the laboratory and the field—including multiple interacting individuals that were first localized and  
 239 cropped from larger, multi-individual images (see “Methods” for details).

240 **An end-to-end pose estimation framework**

241 We provide a full-featured, extensible, and easy-to-use software package that is written entirely in the Python  
242 programming language (Python Software Foundation) and is built on the popular Keras deep-learning package  
243 (*Chollet et al., 2015*)—using TensorFlow as a backend (*Abadi et al., 2015*). Our software is a complete, end-to-  
244 end pipeline (Figure 1) with a custom GUI for creating annotated training data with active learning similar to  
245 *Pereira et al.* (2019; Appendix 3), as well as a flexible pipeline for data augmentation (*Jung 2018*; Appendix 3;  
246 shown in Figure 2), model training and evaluation (Figure 2; Appendix 2), and running inference on new data.  
247 We designed our high-level programming interface using the same guidelines from Keras (*Chollet et al., 2015*)  
248 to allow the user to go from idea to result as quickly as possible, and we organized our software into a Python  
249 module called *DeepPoseKit*. The code, documentation, and examples for our entire software package are freely  
250 available at <https://github.com/jgraving/deeposekit> under a permissive open-source license.

251 **Our pose estimation models**

252 To achieve the goal of “fast animal pose estimation” introduced by *Pereira et al.* (2019), while maintaining  
253 the robust predictive power of models like DeepLabCut (*Mathis et al., 2018*), we implemented two fast pose  
254 estimation models that extend the state-of-the-art model for individual pose estimation introduced by *Newell*  
255 *et al.* (2016) and the current state-of-the art for convolutional regression from *Jégou et al.* (2017). Our model  
256 implementations use fewer parameters than both the DeepLabCut model (*Mathis et al., 2018*) and LEAP model  
257 (*Pereira et al., 2019*) while simultaneously removing many of the limitations of these architectures.

258 In order to limit overparameterization while minimizing performance loss, we designed our models to allow  
259 for multi-scale inference (Appendix 4 Box 1) while optimizing our model hyperparameters for efficiency. Our  
260 first model is a novel implementation of *FC-DenseNet* from *Jégou et al.* (2017; Appendix 4 Box 1) arranged in a  
261 stacked configuration similar to *Newell et al.* (2016; Appendix 5). We call this new model Stacked DenseNet, and  
262 to the best of our knowledge, this is the first implementation of this model architecture in the literature—for  
263 pose estimation or otherwise. Further details for this model are available in Appendix 8. Our second model  
264 is a modified version of the *Stacked Hourglass* model from *Newell et al.* (2016; Appendix 5) with hyperparam-  
265 eters that allow for changing the number of filters in each convolutional block to constrain the number of  
266 parameters—rather than using 256 filters for all layers as described in *Newell et al.* (2016).

267 **Subpixel keypoint prediction on the GPU allows for fast and accurate inference**

268 In addition to implementing our efficient pose estimation models, we developed a new method to process model  
269 outputs to allow for faster, more accurate predictions. When using a fully-convolutional posture estimation  
270 model, the confidence maps produced by the model must be converted into coordinate values for the predictions  
271 to be useful, and there are typically two choices for making this conversion. The first is to move the confidence  
272 maps out of GPU memory and post-process them on the CPU. This solution allows for easy, flexible, and accurate  
273 calculation of the coordinates with subpixel precision (*Insafutdinov et al., 2016*; *Mathis et al., 2018*). However,  
274 CPU processing is not ideal because moving large arrays of data between the GPU and CPU can be costly, and  
275 computation on the CPU is generally slower. The other option is to directly process the confidence maps on the  
276 GPU and then move the coordinate values from the GPU to the CPU. This approach usually means converting  
277 confidence maps to integer coordinates based on the row and column index of the global maximum for each  
278 confidence map (*Pereira et al., 2019*). However, this means that, to achieve a precise estimation, the confidence  
279 maps should be predicted at the full resolution of the input image, or larger, which slows down inference speed.

280 As an alternative to these two strategies, we introduce a new GPU-based convolutional layer that we call  
281 *subpixel maxima*. This layer uses the fast, efficient, image registration algorithm introduced by *Guizar-Sicairos*  
282 *et al.* (2008) to translationally align a centered two-dimensional Gaussian filter to each confidence map via  
283 Fourier-based convolution. The translational shift between the filter and each confidence map allows us to  
284 calculate the coordinates of the global maxima with high speed and subpixel precision. This technique allows  
285 for accurate predictions of keypoint locations even if the model’s confidence maps are dramatically smaller than  
286 the resolution of the input image. We compared the accuracy of our subpixel maxima layer to an integer-based  
287 maxima layer using the fly dataset from *Pereira et al.* (2019) (see “Methods”). We found significant accuracy  
288 improvements across every downsampling configuration (Appendix 1 Figure 1a). Even with confidence maps at  
289  $\frac{1}{8}$  the resolution of the original image, error did not drastically increase compared to full-resolution predictions.  
290 Making predictions for confidence maps at such a downsampled resolution allows us to achieve very fast  
291 inference >1000 Hz while maintaining high accuracy (Appendix 1 Figure 1b).

292 We also provide speed comparisons with the other models we tested and find that our Stacked DenseNet  
293 model with our subpixel peak detection algorithm is faster than the DeepLabCut model (*Mathis et al., 2018*) for  
294 both offline (batch size = 100) and real-time speeds (batch size = 1). While we find that our Stacked DenseNet  
295 model is faster than the LEAP model (*Pereira et al., 2019*) for offline processing (batch size = 100), the LEAP

296 model (*Pereira et al., 2019*) is significantly faster for real-time processing (batch size = 1). Our Stacked Hourglass  
297 model (*Newell et al., 2016*) is about the same or slightly faster than Stacked DenseNet for offline speeds  
298 (batch size = 100), but is much slower for real-time processing (batch size = 1). Achieving fast pose estimation  
299 using CNNs typically relies on massively parallel processing on the GPU with large batches of data or requires  
300 downsampling the images to increase speed, which increases error (*Mathis and Warren, 2018*). These factors  
301 make fast and accurate real-time inference challenging to accomplish. Our Stacked DenseNet model, with a  
302 batch size of one, can run inference at ~30-110Hz—depending on the resolution of the predicted confidence  
303 maps (Appendix 1 Figure 1b). These speeds are faster than the DeepLabCut model (*Mathis et al., 2018*) and  
304 could be further improved by downsampling the input image resolution or reconfiguring the model with fewer  
305 parameters. This allows our methods to be flexibly used for real-time or closed-loop behavioral experiments  
306 with prediction errors similar to current state-of-the-art methods.

### 307 **Learning multi-scale geometry between keypoints improves accuracy and reduces 308 extreme errors**

309 Minimizing extreme prediction errors is important to prevent downstream effects on any further behavioral  
310 analysis (*Seethapathi et al., 2019*)—especially in the case of analyses based on time-frequency transforms like  
311 those from *Berman et al. (2014a, 2016)*; *Klibaite et al. (2017)*; *Todd et al. (2017)*; *Klibaite and Shaevitz (2019)*  
312 and *Pereira et al. (2019)* where high magnitude errors can cause inaccurate behavioral classifications. While  
313 effects of these extreme errors can be minimized using post-hoc filters and smoothing, these post-processing  
314 techniques can remove relevant high-frequency information from time-series data, so this solution is less than  
315 ideal. One way to minimize extreme errors when estimating posture is to incorporate multiple spatial scales  
316 when making predictions (e.g., *Chen et al. 2017*). Our pose estimation models are implicitly capable of using  
317 information from multiple scales (see Appendix 4 Box 1), but there is no explicit signal that optimizes the model  
318 to take advantage of this information when making predictions.

319 To remedy this, we modified the model’s output to predict, in addition to keypoint locations, a hierarchical  
320 graph of edges describing the multi-scale geometry between keypoints—similar to the part affinity fields  
321 described by *Cao et al. (2017)*. This was achieved by adding an extra set of confidence maps to the output where  
322 edges in the postural graph are represented by Gaussian-blurred lines the same width as the Gaussian peaks in  
323 the keypoint confidence maps. Our posture graph output then consists of four levels: (1) a set of confidence  
324 maps for the smallest limb segments in the graph (e.g., foot to ankle, knee to hip, etc.; Figure 2), (2) a set of  
325 confidence maps for individual limbs (e.g., left leg, right arm, etc.; Figure 3), (3) a map with the entire postural  
326 graph, and (4) a fully-integrated map that incorporates the entire posture graph and confidence peaks for all of  
327 the joint locations (Figure 2). Each level of the hierarchical graph is built from lower levels in the output, which  
328 forces the model to learn correlated features across multiple scales when making predictions.

329 We find that training our Stacked DenseNet model to predict a hierarchical posture graph reduces keypoint  
330 prediction error (Appendix 1 Figure 2), and because the feature maps for the posture graph can be removed  
331 from the final output during inference, this effectively improves prediction accuracy for free. Both the mean and  
332 variance of the error distributions were lower when predicting the posture graph, which suggests that learning  
333 multi-scale geometry both decreases error on average and helps to reduce extreme prediction errors. The  
334 overall effect size for this decrease in error is fairly small (<1 pixel average reduction in error), but based on the  
335 results from the zebra dataset, this modification more dramatically improves performance for datasets with  
336 higher-variance images and sparse posture graphs. Predicting the posture graph may be especially useful for  
337 animals with long slender appendages such as insect legs and antennae where prediction errors are likely to  
338 occur due to occlusions and natural variation in the movement of these body parts. These results also suggest  
339 that annotating multiple keypoints to incorporate an explicit signal for multi-scale information may help improve  
340 prediction accuracy for a specific body part of interest.

### 341 **Stacked DenseNet is fast and robust**

342 We benchmarked our new model implementations against the models (*Pereira et al., 2019*) and *Mathis et al.*  
343 (*2018*). We find that our Stacked DenseNet model outperforms both the LEAP model (*Pereira et al., 2019*) and  
344 the DeepLabCut model (*Mathis et al., 2018*) in terms of speed while also achieving much higher accuracy than  
345 the LEAP model (*Pereira et al., 2019*) with similar accuracy to the DeepLabCut model (*Mathis et al. 2018*; Figure  
346 3a). We found that both the Stacked Hourglass and Stacked DenseNet models outperformed the LEAP model  
347 (*Pereira et al., 2019*). Notably our Stacked DenseNet model achieved approximately 2x faster inference speeds  
348 with 3x higher mean accuracy. Not only were our models’ average prediction error significantly improved, but  
349 also, importantly, the variance was lower—indicating that our models produced fewer extreme prediction errors.  
350 At  $\frac{1}{4} \times$  resolution, our Stacked DenseNet model consistently achieved prediction accuracy nearly identical to the  
351 DeepLabCut model (*Mathis et al., 2018*) while running inference at nearly 2x the speed and using only ~5% of

352 the parameters—~1.5 million vs. ~26 million. Detailed results of our model comparisons are shown in Figure  
353 3-Figure supplement 1.

354 While the Stacked DenseNet model used for comparisons is already fast, inference speed could be further  
355 improved by using a  $\frac{1}{8} \times$  output without much increase in error (Appendix 1 Figure 1) or by further adjusting the  
356 hyperparameters to constrain the size of the model. Our Stacked Hourglass implementation followed closely  
357 behind the performance of our Stacked DenseNet model and the DeepLabCut model (*Mathis et al., 2018*) but  
358 consistently performed more poorly than our Stacked DenseNet model in terms of prediction accuracy, so we  
359 excluded this model from further analysis. We were also able to reproduce the results reported by *Pereira*  
360 *et al. (2019)* that the LEAP model and the Stacked Hourglass model (*Newell et al., 2016*) have similar average  
361 prediction error for the fly dataset. However, we also find that the LEAP model (*Pereira et al., 2019*) has much  
362 higher variance, which suggests it is more prone to extreme prediction errors—a problem for further data  
363 analysis.

### 364 **Stacked DenseNet trains quickly and requires few training examples**

365 To further compare models, we used our zebra dataset to assess the training time needed for our Stacked  
366 DenseNet model, the DeepLabCut model (*Mathis et al., 2018*), and the LEAP model (*Pereira et al., 2019*) to  
367 reach convergence as well as the amount of training data needed for each model to generalize to new data  
368 from outside the training set. We find that our Stacked DenseNet model, the DeepLabCut model (*Mathis et al.,*  
369 *2018*), and the LEAP model (*Pereira et al., 2019*) all fully converge in just a few hours and reach reasonably high  
370 accuracy after only an hour of training (Appendix 1 Figure 3). However, it appears that our Stacked DenseNet  
371 model tends to converge to a good minimum faster than both the DeepLabCut model (*Mathis et al., 2018*) and  
372 the LEAP model (*Pereira et al., 2019*).

373 We also show that our Stacked DenseNet model achieves good generalization with few training examples  
374 and without the use of transfer learning (Appendix 1 Figure 4). These results demonstrate that, when combined  
375 with data augmentation, as few as five training examples can be used as an initial training set for labelling  
376 keypoints with active learning (Figure 1). Additionally, because our analysis shows that generalization to new  
377 data plateaus after approximately 100 labeled training examples, it appears that 100 training examples is  
378 a reasonable minimum size for a training set—although the exact number will likely change depending the  
379 variance of the image data being annotated. To further examine the effect of transfer learning on model  
380 generalization, we compared performance between the DeepLabCut model (*Mathis et al., 2018*) initialized with  
381 weights pretrained on the ImageNet database (*Deng et al., 2009*) vs. the same model with randomly-initialized  
382 weights (Appendix 1 Figure 4). As postulated by *Mathis et al. (2018)*, we find that transfer learning does provide  
383 some benefit to the DeepLabCut model’s ability to generalize. However, the effect size of this improvement  
384 is small with a mean reduction in Euclidean error of <0.5 pixel. Together these results indicate that transfer  
385 learning is helpful, but not required, for deep learning models to achieve good generalization with limited  
386 training data.

## 387 **Discussion**

388 Here we have presented a new software toolkit, called DeepPoseKit, for estimating animal posture using deep  
389 learning models. We built on the state-of-the-art for individual pose estimation using convolutional neural  
390 networks to achieve fast inference without reducing accuracy or generalization ability. Our new pose estimation  
391 model, called Stacked DenseNet, offers considerable improvements (Figure 3a; Figure supplement 1) over the  
392 models from *Mathis et al. (2018)* (DeepLabCut) and *Pereira et al. (2019)* (LEAP), and our software framework  
393 also provides a simplified interface (Figure 3b) for using these advanced tools to measure animal behavior  
394 and locomotion. We tested our methods across a range of datasets from controlled laboratory environments  
395 with single individuals to challenging field situations with multiple interacting individuals and variable lighting  
396 conditions. We found that our methods perform well for all of these situations and require few training examples  
397 to achieve good predictive performance on new data—without the use of transfer learning. We ran experiments  
398 to optimize our approach and discovered that some straightforward modifications can greatly improve speed  
399 and accuracy. Additionally, we demonstrated that these modifications improve not just the average error  
400 but also help to reduce extreme prediction errors—a key determinant for the reliability of subsequent statistical  
401 analysis.

402 While our results offer a good-faith comparison of the available methods for animal pose estimation,  
403 there is inherent uncertainty that we have attempted to account for but may still bias our conclusions. For  
404 example, deep learning models are trained using stochastic optimization algorithms that give different results  
405 with each replicate, and the Bayesian statistical methods we use for comparison are explicitly probabilistic in  
406 nature. There is also great variability across hardware and software configurations when using these models  
407 in practice (*Mathis and Warren, 2018*), so performance may change across experimental setups and datasets.

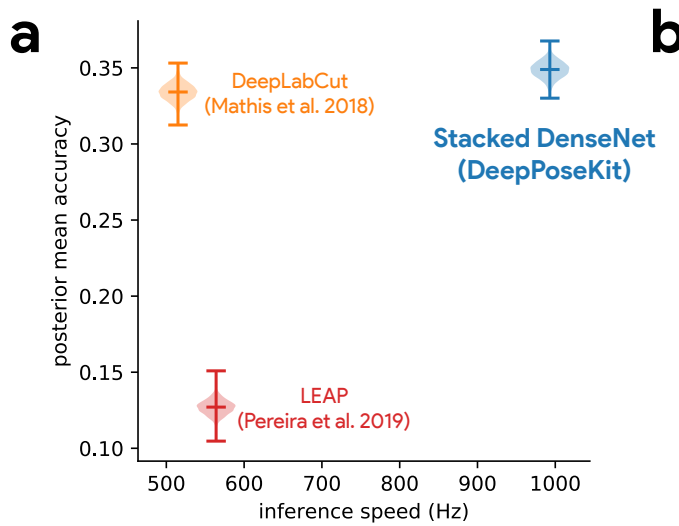


**Figure 3.** Our Stacked DenseNet model estimates posture at approximately 2x—or greater—the speed of the LEAP model (Pereira et al., 2019) and the DeepLabCut model (Mathis et al., 2018) while also achieving similar accuracy to the DeepLabCut model (Mathis et al., 2018)—shown here as mean accuracy ( $1 + \text{Euclidean error}$ )<sup>-1</sup> for our most challenging dataset of multiple interacting Grévy’s zebras (*E. grevyi*) recorded in the wild (a). See Figure 3 supplement 1 for further details. Our software interface is designed to be straightforward but flexible. We include many options for expert users to customize model training with sensible default settings to make pose estimation as easy as possible for beginners. For example, training a model and running inference on new data requires writing only a few lines of code and specifying some basic settings (b).

**Figure 3—Figure supplement 1.** Euclidean error distributions for each model across our three datasets. Letter-value plots (left) show the raw error distributions for each model. Violinplots of the posterior distributions for the mean and variance (right) show statistical differences between the error distributions. Overall the LEAP model (Pereira et al., 2019) was the worst performer on every dataset in terms of both mean and variance. Our Stacked DenseNet model was the best performer for the fly dataset, while our Stacked DenseNet model and the DeepLabCut model (Mathis et al., 2018) both performed equally well on the locust and zebra datasets. The posteriors for the DeepLabCut model (Mathis et al., 2018) and our Stacked DenseNet model are highly overlapping for these datasets, which suggests they are not statistically discernible from one another. Our Stacked Hourglass model (Newell et al., 2016) performed equally to the DeepLabCut model (Mathis et al., 2018) and our Stacked DenseNet model for the locust dataset but performed slightly worse for the fly and zebra datasets.

**b**

```
# initialize, train, and save a model
from deepposekit.io import TrainingGenerator
from deepposekit.models import StackedDenseNet

generator = TrainingGenerator('path/to/data.h5')
model = StackedDenseNet(generator)
model.fit(batch_size=16, n_workers=8)
model.save('path/to/model.h5')

# load the model and run inference on new data
from deepposekit.models import load_model

model = load_model('path/to/model.h5')
new_data = load_new_data('path/to/new/data')
predictions = model.predict(new_data)
```

408 Additionally, we demonstrated that some models may perform better than others for specific applications  
409 (Figure 3 supplement 1), and to account for this, our toolkit offers researchers the ability to choose the model  
410 that best suits their requirements—including the LEAP model (*Pereira et al., 2019*) and the DeepLabCut model  
411 (*Mathis et al., 2018*).

412 We highlighted important considerations when using CNNs for pose estimation and reviewed the progress of  
413 fully-convolutional regression models from the literature. The latest advancements for these models have been  
414 driven mostly by a strategy of adding more connections between layers to increase performance and efficiency  
415 (e.g., *Jégou et al. 2017*). Future progress for this class of models may require better loss functions (*Goodfellow*  
416 *et al., 2014; Johnson et al., 2016a; Chen et al., 2017; Zhang et al., 2018*) that more explicitly model the spatial  
417 dependencies within a scene, models that incorporate the temporal structure of the data (*Seethapathi et al.,*  
418 *2019*), and more mathematically-principled approaches (e.g., *Weigert et al. 2018; Roy et al. 2018*) such as the  
419 application of formal probabilistic concepts (*Kendall and Gal, 2017*) and Bayesian inference at scale (*Tran et al.,*  
420 *2018*).

421 Measuring behavior is a critical factor for many studies in neuroscience (*Krakauer et al., 2017*). Understanding  
422 the connections between brain activity and behavioral output requires detailed and objective descriptions  
423 of body posture that match the richness and resolution neural measurement technologies have provided for  
424 years (*Anderson and Perona, 2014; Berman, 2018; Brown and De Bivort, 2018*), which our methods and other  
425 deep-learning-based tools provide (*Mathis et al., 2018; Pereira et al., 2019*). We have also demonstrated the  
426 possibility that our toolkit could be used for real-time inference, which allows for closed-loop experiments  
427 where sensory stimuli or optogenetic stimulation are controlled in response to behavioral measurements  
428 (e.g., *Bath et al. 2014; Stowers et al. 2017*). Using real-time measurements in conjunction with optogenetics or  
429 thermogenetics may be key to disentangling the causal structure of motor output from the brain—especially  
430 given that recent work has shown an animal's response to optogenetic stimulation can differ depending on the  
431 behavior it is currently performing (*Cande et al., 2018*). Real-time behavioral quantification is also particularly  
432 important as closed-loop virtual reality is quickly becoming an indispensable tool for studying sensorimotor  
433 relationships in individuals and collectives (*Stowers et al., 2017*).

434 Quantifying individual movement is essential for revealing the genetic (*Kain et al., 2012; Brown et al., 2013;*  
435 *Ayroles et al., 2015*) and environmental (*Bierbach et al., 2017; Akhund-Zade et al., 2019; Versace et al., 2019*)  
436 underpinnings of phenotypic variation in behavior—as well as the phylogeny of behavior (e.g., *Berman et al.*  
437 *2014b*). Measuring individual behavioral phenotypes requires tools that are robust, scalable, and easy-to-use,  
438 and our approach offers the ability to quickly and accurately quantify the behavior of many individuals in  
439 great detail. When combined with tools for genetic manipulations (*Ran et al., 2013; Doudna and Charpentier,*  
440 *2014*), high-throughput behavioral experiments (*Alisch et al., 2018; Javer et al., 2018; Werkhoven et al., 2019*),  
441 and behavioral analysis (e.g., *Berman et al. 2014a; Wiltschko et al. 2015*), our methods could help to provide  
442 the data resolution and statistical power needed for dissecting the complex relationships between genes,  
443 environment, and behavioral variation.

444 When used together with other tools for localization and tracking (e.g., *Pérez-Escudero et al. 2014; Crall*  
445 *et al. 2015; Graving 2017; Romero-Ferrero et al. 2019; Wild et al. 2018; Boenisch et al. 2018*), our methods  
446 are capable of reliably measuring posture for multiple interacting individuals. The importance of measuring  
447 detailed representations of individual behavior when studying animal collectives has been well established  
448 (*Strandburg-Peshkin et al., 2013; Rosenthal et al., 2015; Strandburg-Peshkin et al., 2015, 2017*). Estimating  
449 body posture is an essential first step for unraveling the sensory networks that drive group coordination, such  
450 as vision-based networks measured via raycasting (*Strandburg-Peshkin et al., 2013; Rosenthal et al., 2015*).  
451 Additionally, using body pose estimation in combination with computational models of behavior (e.g., *Costa*  
452 *et al. 2019; Wiltschko et al. 2015*) and unsupervised behavioral classification methods (e.g., *Berman et al. 2014a;*  
453 *Pereira et al. 2019*) may allow for further dissection of how information flows through groups by revealing the  
454 networks of behavioral contagion across multiple timescales and sensory modalities. While we have provided a  
455 straightforward solution for applying existing pose estimation methods to measure collective behavior, there  
456 still remain many challenging scenarios where these methods would fail. For example, tracking posture in a  
457 densely-packed bee hive or school of fish would require novel solutions to deal with the 3-D nature of individual  
458 movement, which includes maintaining individual identities and dealing with the resulting occlusions that go  
459 along with imaging these types of biological systems.

460 When combined with unmanned aerial vehicles (UAVs; *Schiffman 2014*) or other field-based imaging (*Fran-*  
461 *cisco et al., 2019*), applying these methods to the study of individuals and groups in the wild can provide  
462 high-resolution behavioral data that goes beyond the capabilities of current GPS and accelerometry-based  
463 technologies (*Nagy et al., 2010, 2013; Kays et al., 2015; Strandburg-Peshkin et al., 2015, 2017; Flack et al.,*  
464 *2018*)—especially for species that are impractical to study with tags or collars. Additionally, by applying these  
465 methods in conjunction with 3-D habitat reconstruction—using techniques from photogrammetry (*Strandburg-*

466 **Peshkin et al., 2017; Francisco et al., 2019**—field-based studies can begin to integrate fine-scale behavioral  
467 measurements with the full 3-D environment in which the behavior evolved. Future advances will likely allow for  
468 the calibration and synchronization of imaging devices across multiple UAVs (e.g. *Price et al. 2018; Saini et al.*  
469 *2019*). This would make it possible to measure the full 3-D posture of wild animals (e.g. *Zuffi et al. 2019*) in  
470 scenarios where fixed camera systems (e.g. *Nath et al. 2019*) would not be tractable, such as during migratory  
471 or predation events. When combined, these technologies could allow researchers to address questions about  
472 the behavioral ecology of animals that were previously impossible to answer.

473 Computer vision algorithms for measuring behavior at the scale of posture have rapidly advanced in a  
474 very short time; nevertheless, the task of pose estimation is far from solved. There are hard limitations to  
475 this current generation of pose estimation methods that are primarily related to the requirement for human  
476 annotations and user-defined keypoints—both in terms of the number of keypoints, the specific body parts  
477 being tracked, and the inherent difficulty of incorporating temporal information into the annotation and training  
478 procedure. Often the body parts chosen for annotation are an obvious fit for the experimental design and have  
479 reliably-visible reference points on the animal’s body that make them easy to annotate. However, in many cases  
480 the required number and type of body parts needed for data analysis may not be obvious—such as in the case  
481 of unsupervised behavior classification methods (*Berman et al., 2014a; Pereira et al., 2019*). Additionally, the  
482 reference points for labeling images with keypoints can be hard to define and consistently annotate across  
483 images, which is often the case for soft or flexible-bodied animals like worms and fish. Moreover, due to the  
484 laborious nature of annotating keypoints, the current generation of methods also rarely takes into account  
485 the natural temporal structure of the data, instead treating each video frame as a statistically independent  
486 event, which can lead to extreme prediction errors (reviewed by *Seethapathi et al. 2019*). Extending these  
487 methods to track the full three-dimensional posture of animals also typically requires the use of multiple  
488 synchronized cameras (*Nath et al., 2019; Günel et al., 2019*), which increases the cost and complexity of  
489 creating an experimental setup, as well as the manual labor required for annotating a training set, which must  
490 include labeled data from every camera view.

491 These limitations make it clear that fundamentally-different methods may be required to move the field  
492 forward. Future pose estimation methods will likely replace human annotations with fully-articulated volumetric  
493 3-D models of the animal’s body (e.g., *Zuffi et al. 2017, 2019*), and the 3-D scene will be learned in an  
494 unsupervised or weakly-supervised way (e.g., *Jaques et al. 2019; Zuffi et al. 2019*), where the shape, position,  
495 and posture of the animal’s body, the camera position and lens parameters, and the background environment  
496 and lighting conditions will all be jointly learned directly from 2-D images by a deep-learning model (*Valentin*  
497 *et al., 2019; Zuffi et al., 2019*). These *inverse graphics models* (*Kulkarni et al., 2015; Sabour et al., 2017; Valentin*  
498 *et al., 2019*) will likely take advantage of recently-developed differentiable graphics engines that allow 3-D  
499 rendering parameters to be straightforwardly controlled using computationally-efficient optimization methods  
500 (*Zuffi et al., 2019; Valentin et al., 2019*). After optimization, the volumetric 3-D timeseries data predicted by the  
501 deep learning model could be used directly for behavioral analysis or specific keypoints or body parts could be  
502 selected for analysis post-hoc. In order to more explicitly incorporate the natural statistical properties of the  
503 data, these models will also likely rely on the use of perceptual (*Johnson et al., 2016a; Zhang et al., 2018; Zuffi*  
504 *et al., 2019*) and adversarial (*Goodfellow et al., 2014; Chen et al., 2017*) loss functions that incorporate spatial  
505 dependencies within the scene rather than modelling each video frame as a set of statistically independent pixel  
506 distributions—as is the case with current methods that use factorized likelihood functions such as pixel-wise  
507 mean squared error (e.g., *Pereira et al. 2019*) or cross-entropy loss (e.g., *Mathis et al. 2018*). Because there  
508 would be limited or no requirement for human-provided labels, these models could also be easily modified to  
509 incorporate the temporal structure of the data using autoregressive representations (e.g., *Van den Oord et al.*  
510 *2016; Oord et al. 2016; Kumar et al. 2019*), rather than modeling the scene in each video frame as a statistically  
511 independent event. Together these advances could lead to larger, higher-resolution, more reliable behavioral  
512 datasets that could revolutionize our understanding of relationships between behavior, the brain, and the  
513 environment.

514 In conclusion, we have presented a new toolkit, called DeepPoseKit, for automatically measuring animal  
515 posture from images. We combined recent advances from the literature to create methods that are fast, robust,  
516 and widely applicable to a range of species and experimental conditions. When designing our framework we em-  
517 phasized usability across the entire software interface, which we expect will help to make these advanced tools  
518 accessible to a wider range of researchers. The fast inference and real-time capabilities of our methods should  
519 also help further reduce barriers to previously intractable questions across many scientific disciplines—including  
520 neuroscience, ethology, and behavioral ecology—both in the laboratory and the field.

521 **Methods**

522 We ran three main experiments to test and optimize our approach. First, we compared our new subpixel  
523 maxima layer to an integer-based global maxima with downsampled outputs ranging from 1x to  $\frac{1}{16}$ x the input  
524 resolution using our Stacked DenseNet model. Next, we tested if training our Stacked DenseNet model to  
525 predict the multi-scale geometry of the posture graph improves accuracy. Finally, we compared our model  
526 implementations of Stacked Hourglass and Stacked DenseNet to the models from *Pereira et al. (2019)* (LEAP)  
527 and *Mathis et al. (2018)* (DeepLabCut), which we also implemented in our framework (see Appendix 8 for  
528 details). We assessed both the inference speed and prediction accuracy of each model as well as training time  
529 and generalization ability. When comparing these models we incorporated the relevant improvements from  
530 our experiments—including subpixel maxima and predicting multi-scale geometry between keypoints—unless  
531 otherwise noted (see Appendix 8).

532 While we do make comparisons to the DeepLabCut model (*Mathis et al., 2018*) we do not use the same  
533 training routine as *Mathis et al. (2018)* and *Nath et al. (2019)*, who use binary cross-entropy loss for optimizing  
534 the confidence maps in addition to the location refinement maps described by *Insafutdinov et al. (2016)*. We  
535 made this modification in order to hold the training routine constant for each model while only varying the  
536 model itself. However, we find that these differences between training routines effectively have no impact on  
537 performance when the models are trained using the same dataset and data augmentations (Appendix 8 Figure  
538 1). We also provide qualitative comparisons to demonstrate that, when trained with our DeepPoseKit framework,  
539 our implementation of the DeepLabCut model (*Mathis et al., 2018*) appears to produce fewer prediction errors  
540 than the original implementation from *Mathis et al. (2018); Nath et al. (2019)* when applied to a novel video  
541 (Appendix 8 Figure 1-Figure supplements 1 and 2; Appendix 8 Figure 1-video 1).

542 **Datasets**

543 We performed experiments using the vinegar or "fruit" fly (*Drosophila melanogaster*) dataset (Figure 3-video 1)  
544 provided by *Pereira et al. (2019)*, and to demonstrate the versatility of our methods we also compared model  
545 performance across two previously unpublished posture data sets from groups of desert locusts (*Schistocerca*  
546 *gregaria*) recorded in a laboratory setting (Figure 3-video 2), and herds of Grévy's zebras (*Equus grevyi*) recorded  
547 in the wild (Figure 3-video 3). The locust and zebra datasets are particularly challenging for pose estimation  
548 as they feature multiple interacting individuals—with focal individuals centered in the frame—and the latter  
549 with highly-variable environments and lighting conditions. These datasets are freely-available from <https://github.com/jgraving/deepposekit-data> (*Graving et al., 2019*).

551 Our locust dataset consisted of a group of 100 locusts in a circular plastic arena 1-m in diameter. The  
552 locust group was recorded from above using a high-resolution camera (Basler ace acA2040-90umNIR) and  
553 video recording system (Motif, loopbio GmbH). Locusts were localized and tracked using 2-D barcode markers  
554 (*Graving, 2017*) attached to the thorax with cyanoacrylate glue, and any missing localizations (<0.02% of the  
555 total dataset) between successful barcode reads were interpolated with linear interpolation. Our zebra dataset  
556 consisted of variably sized groups in the wild recorded from above using a commercially-available quadcopter  
557 drone (DJI Phantom 4 Pro). Individual zebra were localized using custom deep-learning software based on Faster  
558 R-CNN (*Ren et al., 2015*) for predicting bounding boxes. The positions of each zebra were then tracked across  
559 frames using a linear assignment algorithm (*Munkres, 1957*) and data were manually verified for accuracy.

560 After positional tracking, the videos were then cropped using the egocentric coordinates of each individual  
561 and saved as separate videos—one for each individual. The images used for each training set were randomly  
562 selected using the k-means sampling procedure (with k=10) described by *Pereira et al. (2019)* (Appendix 3) to  
563 reduce correlation between sampled images. After annotating the images with keypoints, we rotationally and  
564 translationally aligned the images and keypoints using the central body axis of the animal in each labeled image.  
565 This step allowed us to more easily perform data augmentations (see "Model training") that allow the model to  
566 make accurate predictions regardless of the animal's body size and orientation (see Appendix 6). However, this  
567 preprocessing step is not a strict requirement for training, and there is no requirement for this preprocessing  
568 step when making predictions on new unlabeled data, such as with the methods described by *Pereira et al.*  
569 (*2019*) (Appendix 6). Before training each model we split each annotated dataset into randomly selected training  
570 and validation sets with 90% training examples and 10% validation examples, unless otherwise noted. The  
571 details for each dataset are described in Table 1.

572 **Model training**

573 For each experiment, we set our model hyperparameters to the same configuration for our Stacked DenseNet  
574 and Stacked Hourglass models. Both models were trained with  $\frac{1}{4}$ x resolution outputs and a stack of two  
575 networks with two outputs where loss was applied (see Figure 2). Although our model hyperparameters could  
576 be infinitely adjusted to trade off between speed and accuracy, we compared only one configuration for each of

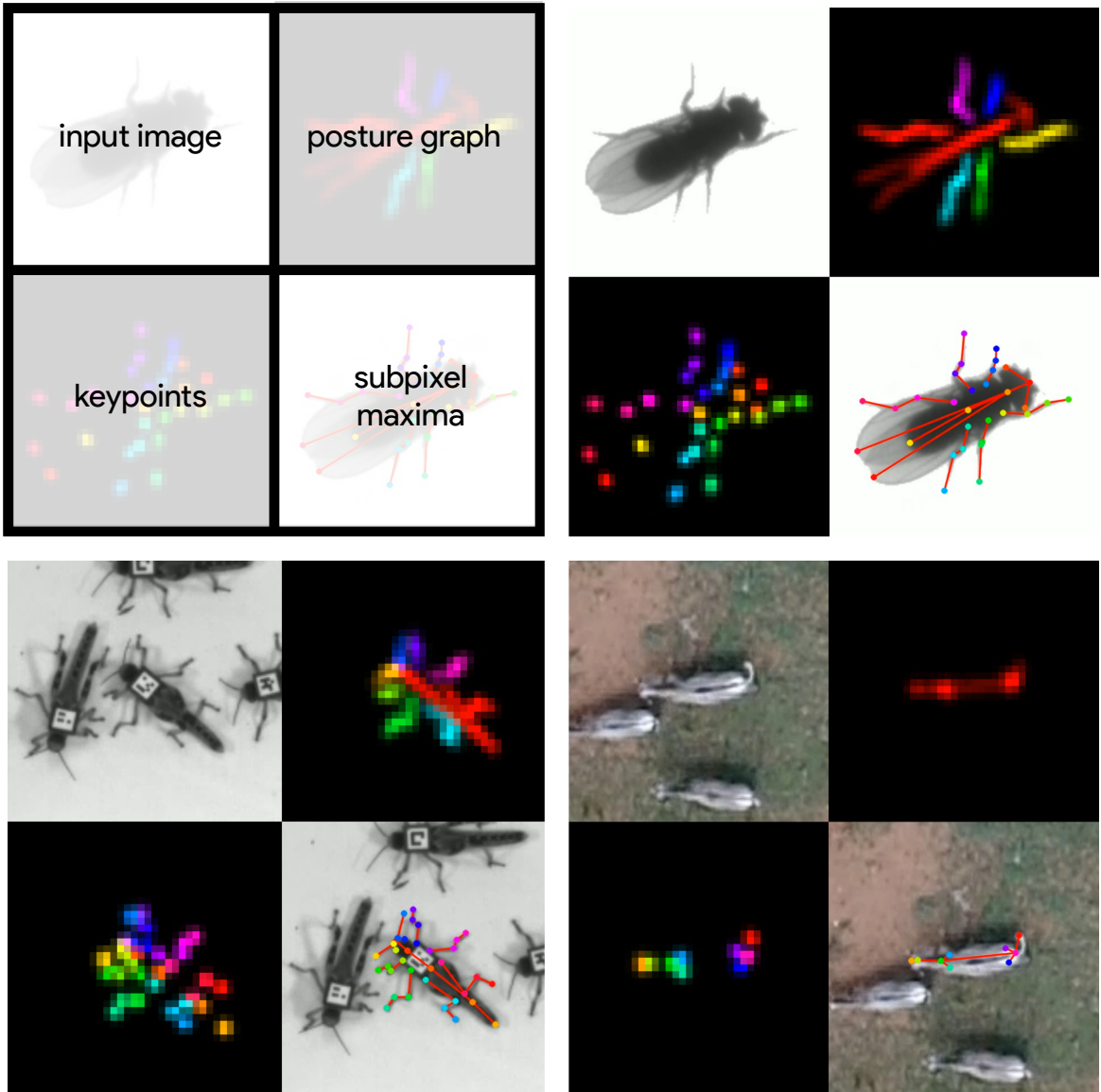


**Figure 4.** A visualization of the datasets we used to evaluate our methods (Table 1). For each dataset, confidence maps for the keypoints (bottom-left) and posture graph (top-right) are illustrated using different colors for each map. These outputs are from our Stacked DenseNet model at  $\frac{1}{4} \times$  resolution.

**Figure 4-video 1.** A video of a behaving fly from *Pereira et al. (2019)* with pose estimation outputs visualized <https://youtu.be/lsnex6k4NRs>

**Figure 4-video 2.** A video of a behaving locust with pose estimation outputs visualized. [https://youtu.be/b0DyyLP\\_Czk](https://youtu.be/b0DyyLP_Czk)

**Figure 4-video 3.** A video of a behaving Grévy's zebra with pose estimation outputs visualized. <https://youtu.be/dSjaphoGHAY>

**Table 1.** Datasets used for model comparisons.

Name	Species	Resolution	# Images	# Keypoints	Individuals	Source
Vinegar fly	<i>Drosophila melanogaster</i>	192×192	1500	32	Single	<i>Pereira et al. (2019)</i>
Desert locust	<i>Schistocerca gregaria</i>	160×160	800	35	Multiple	This paper
Grévy's zebra	<i>Equus grevyi</i>	160×160	900	9	Multiple	This paper

577 our model implementations. These results are not meant to be an exhaustive search of model configurations as  
578 the best configuration will depend on the application. The details of the hyperparameters we used for each  
579 model are described in Appendix 8.

580 To make our posture estimation tasks closer to realistic conditions, incorporate prior information (Appendix  
581 3), and properly demonstrate the robustness of our methods to rotation, translation, scale, and noise, we  
582 applied various augmentations to each data set during training (Figure 2). All models were trained using data  
583 augmentations that included random flipping, or mirroring, along both the horizontal and vertical image axes  
584 with each axis being independently flipped by drawing from a Bernoulli distribution (with  $p = 0.5$ ); random  
585 rotations around the center of the image drawn from a uniform distribution in the range [-180°, +180°]; random  
586 scaling drawn from a uniform distribution in the range [90%, 110%] for flies and locusts and [75%, 125%] for  
587 zebras (to account for greater size variation in the data set); and random translations along the horizontal and  
588 vertical axis independently drawn from a uniform distribution with the range [-5%, +5%]—where percentages  
589 are relative to the original image size. After performing these spatial augmentations we also applied a variety of  
590 noise augmentations that included additive noise—i.e., adding or subtracting randomly-selected values to pixels;  
591 dropout—i.e., setting individual pixels or groups of pixels to a randomly-selected value; blurring or sharpening—  
592 i.e., changing the composition of spatial frequencies; and contrast ratio augmentations—i.e, changing the ratio  
593 between the highest pixel value and lowest pixel value in the image. These augmentations help to further  
594 ensure robustness to shifts in lighting, noise, and occlusions. See Appendix 3 for further discussion on data  
595 augmentation.

596 We trained our models (Figure 2) using mean squared error loss optimized using the ADAM optimizer  
597 (*Kingma and Ba, 2014*) with a learning rate of  $1 \times 10^{-3}$  and a batch size of 16. We lowered the learning rate by a  
598 factor of 5 each time the validation loss did not improve by more than  $1 \times 10^{-3}$  for 10 epochs. We considered  
599 models to be converged when the validation loss stopped improving for 50 epochs, and we calculated validation  
600 error as the Euclidean distance between predicted and ground-truth image coordinates for only the best  
601 performing version of the model, which we evaluated at the end of each epoch during optimization. We  
602 performed this procedure five times for each experiment and randomly selected a new validation set for each  
603 replicate.

## 604 **Model evaluation**

605 Machine learning models are typically evaluated for their ability to generalize to new data, known as *predictive*  
606 *performance*, using a held-out *test set*—a subsample of annotated data that is not used for training or validation.  
607 However, due to the small size of the datasets used for making comparisons, we elected to use only a validation  
608 set for model evaluation, as using an overly small training or test set can bias assessments of a model’s predictive  
609 performance (*Kuhn and Johnson, 2013*). Generally a test set is used to avoid biased performance measures  
610 caused by overfitting the model hyperparameters to the validation set. However, we did not adjust our model  
611 architecture to achieve better performance on our validation set—only to achieve fast inference speeds. While  
612 we did use validation error to decide when to lower the learning rate during training and when to stop training,  
613 lowering the learning rate in this way should have no effect on the generalization ability of the model, and  
614 because we heavily augment our training set during optimization—forcing the model to learn a much larger  
615 data distribution than what is included in the training and validation sets—overfitting to the validation set is  
616 unlikely. We also demonstrate the generality of our results for each experiment by randomly selecting a new  
617 validation set with each replicate. All of these factors make the Euclidean error for the unaugmented validation  
618 set a reasonable measure of the predictive performance for each model.

619 The inference speed for each model was assessed by running predictions on 100,000 randomly generated  
620 images with a batch size of 1 for real-time speeds and a batch size of 100 for offline speeds, unless otherwise  
621 noted. Our hardware consisted of a Dell Precision Tower 7910 workstation (Dell, Inc.) running Ubuntu Linux  
622 v18.04 with 2x Intel Xeon E5-2623 v3 CPUs (8 cores, 16 threads at 3.00GHz), 64GB of RAM, a Quadro P6000 GPU  
623 and a Titan Xp GPU (NVIDIA Corporation). We used both GPUs (separately) for training models and evaluating  
624 predictive performance, but we only used the faster Titan Xp GPU for benchmarking inference speeds and  
625 training time. While the hardware we used for development and testing is on the high-end of the current  
626 performance spectrum, there is no requirement for this level of performance, and our software can easily be  
627 run on lower-end hardware. We evaluated inference speeds on multiple consumer-grade desktop computers  
628 and found similar performance ( $\pm 10\%$ ) when using the same GPU; however, training speed depends more  
629 heavily other hardware components like the CPU and hard disk.

## 630 **Assessing prediction accuracy with Bayesian inference**

631 To more rigorously assess performance differences between models, we parameterized the Euclidean error  
632 distribution for each experiment by fitting a Bayesian linear model with a Gamma-distributed likelihood function.

633 This model takes the form:

$$\begin{aligned} p(y|X, \theta_\mu, \theta_\phi) &\sim \text{Gamma}(\alpha, \beta) \\ \alpha &= \mu^2 \phi^{-1} \\ \beta &= \mu \phi^{-1} \\ \mu &= h(X\theta_\mu) \\ \phi &= h(X\theta_\phi) \end{aligned}$$

634 where  $X$  is the design matrix composed of binary indicator variables for each pose estimation model,  $\theta_\mu$   
635 and  $\theta_\phi$  are vectors of intercepts,  $h(\cdot)$  is the softplus function (**Dugas et al., 2001**)—or  $h(x) = \log(1 + e^x)$ —used to  
636 enforce positivity of  $\mu$  and  $\phi$ , and  $y$  is the Euclidean error of the pose estimation model. Parameterizing our  
637 error distributions in this way allows us to calculate the posterior distributions for the mean  $E[y] = \alpha\beta^{-1} \equiv \mu$  and  
638 variance  $\text{Var}[y] = \alpha\beta^{-2} \equiv \phi$ . This parameterization then provides us with a statistically rigorous way to assess  
639 differences in model accuracy in terms of both central tendency and spread—accounting for both epistemic  
640 uncertainty (unknown unknowns; e.g., parameter uncertainty) and aleatoric uncertainty (known unknowns; e.g.,  
641 data variance). Details of how we fitted these models can be found in Appendix 7.

## 642 Author contributions

643 J.M.G and I.D.C conceived the idea for the project. J.M.G. and D.C. developed the software with input from H.N.  
644 J.M.G implemented the pose estimation models and developed the subpixel maxima algorithm. J.M.G. and D.C.  
645 developed the annotation GUI, data augmentation pipeline, and wrote the documentation. J.M.G., D.C. and H.N.  
646 designed the experiments. J.M.G. and D.C. ran the experiments. B.R.C., B.K., J.M.G., and I.D.C. conceived the idea  
647 to apply posture tracking to zebras. B.R.C. and B.K. provided the annotated zebra posture data. B.K., and L.L.  
648 helped with initial testing and improvement of the software interface. L.L. also made significant contributions to  
649 an earlier version of the manuscript. J.M.G. fit the linear models and made the figures. J.M.G. wrote the initial  
650 draft of the manuscript with input from H.N. and D.C., and all authors helped revise the manuscript.

## 651 Acknowledgements

652 We are indebted to Talmo Pereira et al. and A. Mathis et al. for making their software open-source and  
653 freely-available—this project would not have been possible without them. We also thank M. Mathis and A.  
654 Mathis for their comments, which greatly improved the manuscript. We thank François Chollet, the Keras  
655 and TensorFlow teams, and Alexander Jung for their open source contributions, which provided the core  
656 programming interface for our work. We thank A. Strandburg-Peshkin, Vivek H. Sridhar, Michael L. Smith, and  
657 Joseph B. Bak-Coleman for their helpful discussions on the project and comments on the manuscript. We  
658 also thank M.L.S. for the use of his GPU. We thank Felicitas Oehler for annotating the zebra posture data and  
659 Chiara Hirschhorn for assistance with filming the locusts and annotating the locust posture data. We thank  
660 Alex Brutel, Christine Bauer, Jayme Weglarzki, Dominique Leo, Markus Miller and loobio GmbH for providing  
661 technical support. We acknowledge the NVIDIA Corporation for their generous donations to our research. This  
662 project received funding from the European Union's Horizon 2020 research and innovation programme under  
663 the Marie Skłodowska-Curie grant agreement No. 748549. B.R.C. acknowledges support from the University  
664 of Konstanz Zukunftskolleg's Investment Grant program. I.D.C. acknowledges support from NSF Grant IOS-  
665 1355061, Office of Naval Research Grants N00014-09-1-1074 and N00014-14-1-0635, Army Research Office  
666 Grants W911NG-11-1-0385 and W911NF14-1-0431, the Struktur-und Innovationsfonds fur die Forschung of the  
667 State of Baden-Württemberg, the DFG Centre of Excellence 2117 "Centre for the Advanced Study of Collective  
668 Behaviour" (ID: 422037984), and the Max Planck Society.

## 669 Animal Ethics Statement

670 All procedures for collecting the zebra (*E. grevyi*) dataset were reviewed and approved by Ethikrat, the inde-  
671 pendent Ethics Council of the Max Planck Society. The zebra dataset was collected with the permission of  
672 Kenya's National Commission for Science, Technology and Innovation (NACOSTI/P/17/59088/15489 and NA-  
673 COSTI/P/18/59088/21567) using drones operated by B.R.C. with the permission of the Kenya Civil Aviation  
674 Authority (authorization numbers: KCAA/OPS/2117/4 Vol. 2 (80), KCAA/OPS/2117/4 Vol. 2 (81), KCAA/OPS/2117/5  
675 (86) and KCAA/OPS/2117/5 (87); RPAS Operator Certificate numbers: RPA/TP/0005 AND RPA/TP/000-0009).

## References

- 676     **Abadi M, Agarwal A, Barham P, Brevdo E, Chen Z, Citro C, Corrado GS, Davis A, Dean J, Devin M, Ghemawat S, Goodfellow I, Harp  
677       A, Irving G, Isard M, Jia Y, Jozefowicz R, Kaiser L, Kudlur M, Levenberg J, et al., TensorFlow: Large-Scale Machine Learning on  
678       Heterogeneous Systems; 2015. <https://www.tensorflow.org/>, software available from tensorflow.org.**
- 680     **Akhund-Zade J, Ho S, O'Leary C, de Bivort B.** The effect of environmental enrichment on behavioral variability depends on  
681       genotype, behavior, and type of enrichment. *Journal of Experimental Biology*. 2019; <https://jeb.biologists.org/content/early/2019/08/14/jeb.202234>; doi: 10.1242/jeb.202234.
- 683     **Alisch T, Crall JD, Kao AB, Zucker D, de Bivort BL.** MAPLE (modular automated platform for large-scale experiments), a robot for  
684       integrated organism-handling and phenotyping. *eLife*. 2018; 7:e37166.
- 685     **Anderson DJ, Perona P.** Toward a science of computational ethology. *Neuron*. 2014; 84(1):18–31.
- 686     **Andriluka M, Iqbal U, Insafutdinov E, Pishchulin L, Milan A, Gall J, Schiele B.** Posetrack: A benchmark for human pose estimation  
687       and tracking. In: *Proceedings of the IEEE Conference on Computer Vision and Pattern Recognition*; 2018. p. 5167–5176.
- 688     **Andriluka M, Pishchulin L, Gehler P, Schiele B.** 2D Human Pose Estimation: New Benchmark and State of the Art Analysis. In:  
689       *IEEE Conference on Computer Vision and Pattern Recognition (CVPR)*; 2014..
- 690     **Ayinde BO, Zurada JM.** Building efficient convnets using redundant feature pruning. *arXiv preprint arXiv:180207653*. 2018; .
- 691     **Ayroles JF, Buchanan SM, O'Leary C, Skutt-Kakaria K, Grenier JK, Clark AG, Hartl DL, de Bivort BL.** Behavioral idiosyncrasy reveals  
692       genetic control of phenotypic variability. *Proceedings of the National Academy of Sciences*. 2015; 112(21):6706–6711.
- 693     **Badrinarayanan V, Kendall A, Cipolla R.** SegNet: A Deep Convolutional Encoder-Decoder Architecture for Image Segmentation.  
694       CoRR. 2015; abs/1511.00561. <http://arxiv.org/abs/1511.00561>.
- 695     **Bath DE, Stowers JR, Hörmann D, Poehlmann A, Dickson BJ, Straw AD.** FlyMAD: rapid thermogenetic control of neuronal activity  
696       in freely walking Drosophila. *Nature methods*. 2014; 11(7):756.
- 697     **Berman GJ.** Measuring behavior across scales. *BMC biology*. 2018; 16(1):23.
- 698     **Berman GJ, Bialek W, Shaevitz JW.** Predictability and hierarchy in Drosophila behavior. *Proceedings of the National Academy of  
699       Sciences*. 2016; 113(42):11943–11948.
- 700     **Berman GJ, Choi DM, Bialek W, Shaevitz JW.** Mapping the stereotyped behaviour of freely moving fruit flies. *Journal of The Royal  
701       Society Interface*. 2014; 11(99):20140672.
- 702     **Berman GJ, Choi DM, Bialek W, Shaevitz JW.** Mapping the structure of drosophilid behavior. *bioRxiv*. 2014; p. 002873.
- 703     **Bierbach D, Laskowski KL, Wolf M.** Behavioural individuality in clonal fish arises despite near-identical rearing conditions.  
704       *Nature communications*. 2017; 8:15361.
- 705     **Boenisch F, Rosemann B, Wild B, Dormagen D, Wario F, Landgraf T.** Tracking All Members of a Honey Bee Colony Over Their  
706       Lifetime Using Learned Models of Correspondence. *Frontiers in Robotics and AI*. 2018; 5:35. <https://www.frontiersin.org/article/10.3389/frobt.2018.00035>; doi: 10.3389/frobt.2018.00035.
- 708     **Brown AE, De Bivort B.** Ethology as a physical science. *Nature Physics*. 2018; p. 1.
- 709     **Brown AE, Yemini EI, Grundy LJ, Jucikas T, Schafer WR.** A dictionary of behavioral motifs reveals clusters of genes affecting  
710       Caenorhabditis elegans locomotion. *Proceedings of the National Academy of Sciences*. 2013; 110(2):791–796.
- 711     **Cande J, Namiki S, Qiu J, Korff W, Card GM, Shaevitz JW, Stern DL, Berman GJ.** Optogenetic dissection of descending behavioral  
712       control in Drosophila. *Elife*. 2018; 7:e34275.
- 713     **Cao Z, Simon T, Wei SE, Sheikh Y.** Realtime multi-person 2d pose estimation using part affinity fields. In: *Proceedings of the IEEE  
714       Conference on Computer Vision and Pattern Recognition*; 2017. p. 7291–7299.
- 715     **Carpenter B, Lee D, Brubaker MA, Riddell A, Gelman A, Goodrich B, Guo J, Hoffman M, Betancourt M, Li P.** Stan: A Probabilistic  
716       Programming Language. *J Stat Softw*. 2017; .
- 717     **Cauchy A.** Méthode générale pour la résolution des systèmes d'équations simultanées. *Comp Rend Sci Paris*. 1847; 25(1847):536–  
718       538.
- 719     **Chen Y, Shen C, Wei XS, Liu L, Yang J.** Adversarial posenet: A structure-aware convolutional network for human pose estimation.  
720       In: *Proceedings of the IEEE International Conference on Computer Vision*; 2017. p. 1212–1221.
- 721     **Chollet F, et al.** Keras. GitHub; 2015. <https://github.com/fchollet/keras>.
- 722     **Chollet F.** Xception: Deep learning with depthwise separable convolutions. In: *Proceedings of the IEEE conference on computer  
723       vision and pattern recognition*; 2017. p. 1251–1258.

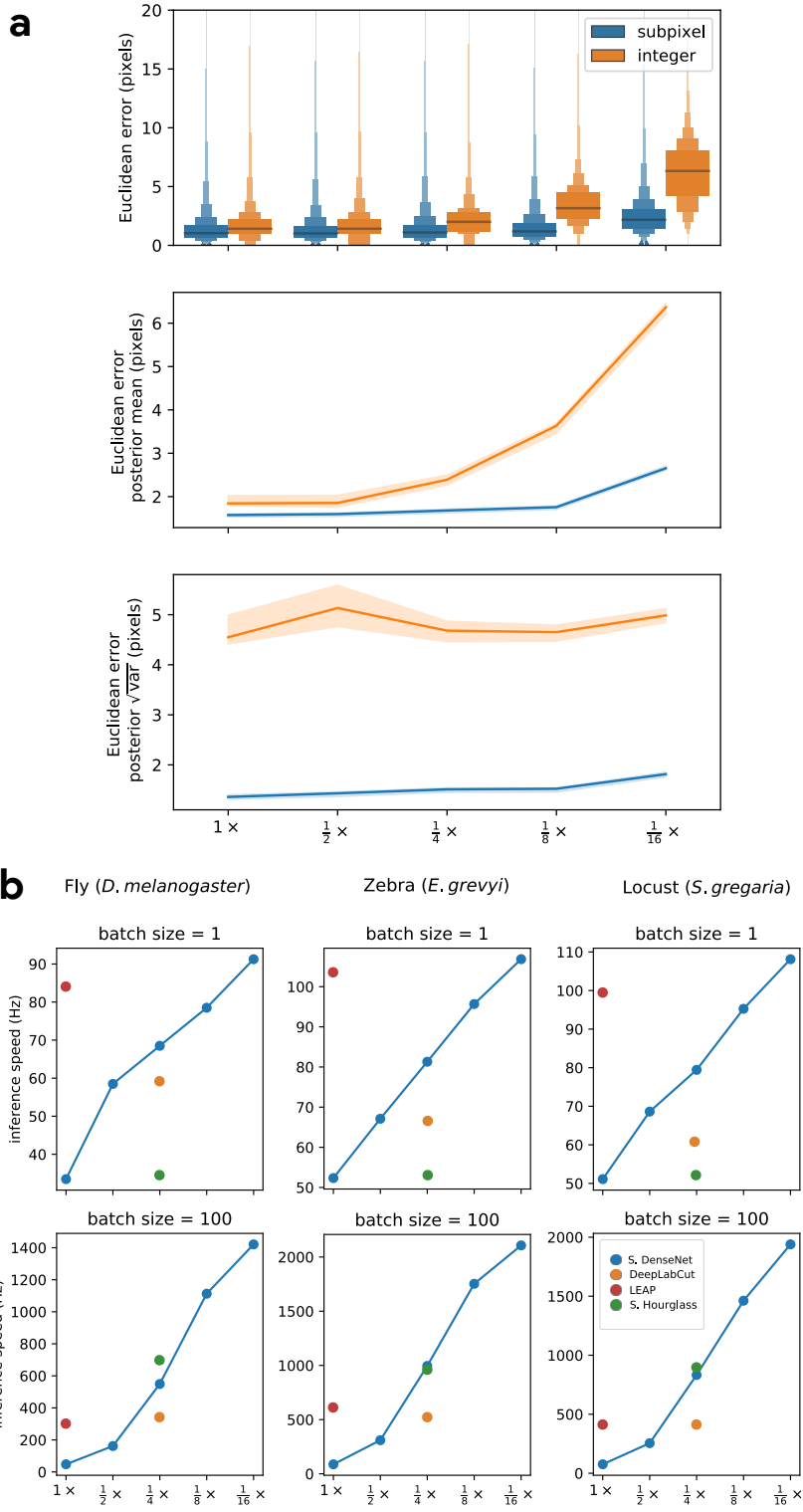
- 724 Costa AC, Ahamed T, Stephens GJ. Adaptive, locally linear models of complex dynamics. Proceedings of the National Academy of Sciences. 2019; 116(5):1501–1510. <https://www.pnas.org/content/116/5/1501>, doi: 10.1073/pnas.1813476116.
- 725
- 726 Crall JD, Gravish N, Mountcastle AM, Combes SA. BEEtag: a low-cost, image-based tracking system for the study of animal behavior and locomotion. PloS one. 2015; 10(9):e0136487.
- 727
- 728 Dell AI, Bender JA, Branson K, Couzin ID, de Polavieja GG, Noldus LP, Pérez-Escudero A, Perona P, Straw AD, Wikelski M, et al. Automated image-based tracking and its application in ecology. Trends in ecology & evolution. 2014; 29(7):417–428.
- 729
- 730 Deng J, Dong W, Socher R, Li LJ, Li K, Fei-Fei L. Imagenet: A large-scale hierarchical image database. . 2009; .
- 731 Doudna JA, Charpentier E. The new frontier of genome engineering with CRISPR-Cas9. Science. 2014; 346(6213):1258096.
- 732 Duane S, Kennedy AD, Pendleton BJ, Roweth D. Hybrid Monte Carlo. Phys Lett B. 1987; 195(2):216–222.
- 733 Dugas C, Bengio Y, Bélisle F, Nadeau C, Garcia R. Incorporating second-order functional knowledge for better option pricing. In: *Advances in neural information processing systems*; 2001. p. 472–478.
- 734
- 735 Flack A, Nagy M, Fiedler W, Couzin ID, Wikelski M. From local collective behavior to global migratory patterns in white storks. Science. 2018; 360(6391):911–914.
- 736
- 737 Francisco FA, Nührenberg P, Jordan AL. A low-cost, open-source framework for tracking and behavioural analysis of animals in aquatic ecosystems. bioRxiv. 2019; <https://www.biorxiv.org/content/early/2019/03/09/571232>, doi: 10.1101/571232.
- 738
- 739 Goodfellow I, Bengio Y, Courville A. Deep learning. MIT press; 2016.
- 740 Goodfellow I, Pouget-Abadie J, Mirza M, Xu B, Warde-Farley D, Ozair S, Courville A, Bengio Y. Generative adversarial nets. In: *Advances in neural information processing systems*; 2014. p. 2672–2680.
- 741
- 742 Graving JM, pinpoint: behavioral tracking using 2D barcode tags v0.0.1-alpha; 2017. <https://doi.org/10.5281/zenodo.1008970>, doi: 10.5281/zenodo.1008970.
- 743
- 744 Graving JM, Chae D, Naik H, Li L, Koger B, Costelloe BR, Couzin ID, Example Datasets for DeepPoseKit; 2019. <https://doi.org/10.5281/zenodo.3366908>, doi: 10.5281/zenodo.3366908.
- 745
- 746 Guijar-Sicairos M, Thurman ST, Fienup JR. Efficient subpixel image registration algorithms. Optics letters. 2008; 33(2):156–158.
- 747
- 748 Günel S, Rhodin H, Morales D, Campagnolo J, Ramdya P, Fua P. DeepFly3D: A deep learning-based approach for 3D limb and appendage tracking in tethered, adult Drosophila. bioRxiv. 2019; p. 640375.
- 749
- 750 He K, Zhang X, Ren S, Sun J. Deep residual learning for image recognition. In: *Proceedings of the IEEE conference on computer vision and pattern recognition*; 2016. p. 770–778.
- 751 Hoffman MD, Gelman A. The No-U-Turn sampler: adaptively setting path lengths in Hamiltonian Monte Carlo. Journal of Machine Learning Research. 2014; 15(1):1593–1623.
- 752
- 753 Huang G, Liu Z, Van Der Maaten L, Weinberger KQ. Densely connected convolutional networks. In: *Proceedings of the IEEE conference on computer vision and pattern recognition*; 2017. p. 4700–4708.
- 754
- 755 Huang J, Rathod V, Sun C, Zhu M, Korattikara A, Fathi A, Fischer I, Wojna Z, Song Y, Guadarrama S, et al. Speed/accuracy trade-offs for modern convolutional object detectors. In: *Proceedings of the IEEE conference on computer vision and pattern recognition*; 2017. p. 7310–7311.
- 756
- 757
- 758 Insafutdinov E, Pishchulin L, Andres B, Andriluka M, Schiele B. Deepcut: A deeper, stronger, and faster multi-person pose estimation model. In: *European Conference on Computer Vision* Springer; 2016. p. 34–50.
- 759
- 760 Iqbal U, Milan A, Gall J. Posetrack: Joint multi-person pose estimation and tracking. In: *Proceedings of the IEEE Conference on Computer Vision and Pattern Recognition*; 2017. p. 2011–2020.
- 761
- 762 Jaques M, Burke M, Hospedales T. Physics-as-Inverse-Graphics: Joint Unsupervised Learning of Objects and Physics from Video. arXiv preprint arXiv:190511169. 2019; .
- 763
- 764 Javer A, Currie M, Lee CW, Hokanson J, Li K, Martineau CN, Yemini E, Grundy LJ, Li C, Ch'ng Q, et al. An open-source platform for analyzing and sharing worm-behavior data. Nature methods. 2018; 15(9):645.
- 765
- 766 Jégou S, Drozdzal M, Vázquez D, Romero A, Bengio Y. The One Hundred Layers Tiramisu: Fully Convolutional DenseNets for Semantic Segmentation. CoRR. 2017; abs/1611.09326. <http://arxiv.org/abs/1611.09326>.
- 767
- 768 Johnson J, Alahi A, Fei-Fei L. Perceptual losses for real-time style transfer and super-resolution. In: *European conference on computer vision* Springer; 2016. p. 694–711.
- 769
- 770 Johnson M, Duvenaud DK, Wiltschko A, Adams RP, Datta SR. Composing graphical models with neural networks for structured representations and fast inference. In: *Advances in neural information processing systems*; 2016. p. 2946–2954.
- 771

- 772 Jolles JW, Boogert NJ, Sridhar VH, Couzin ID, Manica A. Consistent individual differences drive collective behavior and group  
773 functioning of schooling fish. *Current Biology*. 2017; 27(18):2862–2868.
- 774 Jung A, imgaug. GitHub; 2018. <https://github.com/aleju/imgaug>.
- 775 Kain J, Stokes C, Gaudry Q, Song X, Foley J, Wilson R, De Bivort B. Leg-tracking and automated behavioural classification in  
776 Drosophila. *Nature communications*. 2013; 4:1910.
- 777 Kain JS, Stokes C, de Bivort BL. Phototactic personality in fruit flies and its suppression by serotonin and white. *Proceedings of  
778 the National Academy of Sciences*. 2012; 109(48):19834–19839.
- 779 Kays R, Crofoot MC, Jetz W, Wikelski M. Terrestrial animal tracking as an eye on life and planet. *Science*. 2015; 348(6240):aaa2478.
- 780 Ke L, Chang MC, Qi H, Lyu S. Multi-Scale Structure-Aware Network for Human Pose Estimation. In: *The European Conference on  
781 Computer Vision (ECCV)*; 2018. .
- 782 Kendall A, Gal Y. What uncertainties do we need in bayesian deep learning for computer vision? In: *Advances in neural  
783 information processing systems*; 2017. p. 5574–5584.
- 784 Kiefer J, Wolfowitz J, et al. Stochastic estimation of the maximum of a regression function. *The Annals of Mathematical Statistics*.  
785 1952; 23(3):462–466.
- 786 Kingma DP, Ba J. Adam: A method for stochastic optimization. arXiv preprint arXiv:14126980. 2014; .
- 787 Klambauer G, Unterthiner T, Mayr A, Hochreiter S. Self-normalizing neural networks. In: *Advances in neural information  
788 processing systems*; 2017. p. 971–980.
- 789 Klibaite U, Berman GJ, Cande J, Stern DL, Shaevitz JW. An unsupervised method for quantifying the behavior of paired animals.  
790 *Physical biology*. 2017; 14(1):015006.
- 791 Klibaite U, Shaevitz JW. Interacting fruit flies synchronize behavior. bioRxiv. 2019; p. 545483.
- 792 Krakauer JW, Ghazanfar AA, Gomez-Marin A, MacIver MA, Poeppel D. Neuroscience needs behavior: correcting a reductionist  
793 bias. *Neuron*. 2017; 93(3):480–490.
- 794 Kuhn M, Johnson K. Applied predictive modeling, vol. 26. Springer; 2013.
- 795 Kulkarni TD, Whitney WF, Kohli P, Tenenbaum J. Deep convolutional inverse graphics network. In: *Advances in neural information  
796 processing systems*; 2015. p. 2539–2547.
- 797 Kumar M, Babaeizadeh M, Erhan D, Finn C, Levine S, Dinh L, Kingma D. VideoFlow: A flow-based generative model for video.  
798 arXiv preprint arXiv:190301434. 2019; .
- 799 LeCun Y, Bengio Y, Hinton G. Deep learning. *nature*. 2015; 521(7553):436.
- 800 Li H, Xu Z, Taylor G, Studer C, Goldstein T. Visualizing the loss landscape of neural nets. In: *Advances in Neural Information  
801 Processing Systems*; 2018. p. 6391–6401.
- 802 Long J, Shelhamer E, Darrell T. Fully convolutional networks for semantic segmentation. In: *Proceedings of the IEEE conference on  
803 computer vision and pattern recognition*; 2015. p. 3431–3440.
- 804 Markowitz JE, Gillis WF, Beron CC, Neufeld SQ, Robertson K, Bhagat ND, Peterson RE, Peterson E, Hyun M, Linderman SW, et al.  
805 The striatum organizes 3D behavior via moment-to-moment action selection. *Cell*. 2018; 174(1):44–58.
- 806 Mathis A, Mamidanna P, Cury KM, Abe T, Murthy VN, Mathis MW, Bethge M. DeepLabCut: markerless pose estimation of user-  
807 defined body parts with deep learning. *Nature Neuroscience*. 2018; <https://www.nature.com/articles/s41593-018-0209-y>.
- 808 Mathis A, Warren RA. On the inference speed and video-compression robustness of DeepLabCut. bioRxiv. 2018; <https://www.biorxiv.org/content/early/2018/10/30/457242>, doi: 10.1101/457242.
- 810 Mendes CS, Bartos I, Akay T, Márka S, Mann RS. Quantification of gait parameters in freely walking wild type and sensory  
811 deprived Drosophila melanogaster. *elife*. 2013; 2:e00231.
- 812 Munkres J. Algorithms for the assignment and transportation problems. *Journal of the society for industrial and applied  
813 mathematics*. 1957; 5(1):32–38.
- 814 Nagy M, Akos Z, Biro D, Vicsek T. Hierarchical group dynamics in pigeon flocks. *Nature*. 2010; 464(7290):890.
- 815 Nagy M, Vásárhelyi G, Pettit B, Roberts-Mariani I, Vicsek T, Biro D. Context-dependent hierarchies in pigeons. *Proceedings of the  
816 National Academy of Sciences*. 2013; 110(32):13049–13054.
- 817 Nath T, Mathis A, Chen AC, Patel A, Bethge M, Mathis MW. Using DeepLabCut for 3D markerless pose estimation across species  
818 and behaviors. *Nature protocols*. 2019; .

- 819 Newell A, Yang K, Deng J. Stacked Hourglass Networks for Human Pose Estimation. In: *Computer Vision - ECCV 2016 - 14th European Conference, Amsterdam, The Netherlands, October 11-14, 2016, Proceedings, Part VIII*; 2016. p. 483–499. doi: 10.1007/978-3-319-46484-8\_29.
- 822 Van den Oord A, Kalchbrenner N, Espeholt L, Vinyals O, Graves A, et al. Conditional image generation with pixelcnn decoders. In: *Advances in neural information processing systems*; 2016. p. 4790–4798.
- 824 Ord Avd, Dieleman S, Zen H, Simonyan K, Vinyals O, Graves A, Kalchbrenner N, Senior A, Kavukcuoglu K. Wavenet: A generative model for raw audio. arXiv preprint arXiv:160903499. 2016; .
- 826 Pereira TD, Aldarondo DE, Willmore L, Kislin M, Wang SSH, Murthy M, Shaevitz JW. Fast animal pose estimation using deep neural networks. *Nature methods*. 2019; 16(1):117.
- 828 Pérez-Escudero A, Vicente-Page J, Hinz RC, Arganda S, De Polavieja GG. idTracker: tracking individuals in a group by automatic identification of unmarked animals. *Nature methods*. 2014; 11(7):743.
- 830 Pratt LY. Discriminability-based transfer between neural networks. In: *Advances in neural information processing systems*; 1993. p. 204–211.
- 832 Prechelt L. Automatic early stopping using cross validation: quantifying the criteria. *Neural Networks*. 1998; 11(4):761–767.
- 833 Price E, Lawless G, Ludwig R, Martinovic I, Bülthoff HH, Black MJ, Ahmad A. Deep neural network-based cooperative visual tracking through multiple micro aerial vehicles. *IEEE Robotics and Automation Letters*. 2018; 3(4):3193–3200.
- 835 Ran FA, Hsu PD, Wright J, Agarwala V, Scott DA, Zhang F. Genome engineering using the CRISPR-Cas9 system. *Nature protocols*. 2013; 8(11):2281.
- 837 Ren S, He K, Girshick R, Sun J. Faster r-cnn: Towards real-time object detection with region proposal networks. In: *Advances in neural information processing systems*; 2015. p. 91–99.
- 839 Robbins H, Monro S. A stochastic approximation method. *The annals of mathematical statistics*. 1951; p. 400–407.
- 840 Romero-Ferrero F, Bergomi MG, Hinz RC, Heras FJ, de Polavieja GG. idtracker. ai: tracking all individuals in small or large collectives of unmarked animals. *Nature methods*. 2019; 16(2):179.
- 842 Ronneberger O, Fischer P, Brox T. U-net: Convolutional networks for biomedical image segmentation. In: *International Conference on Medical image computing and computer-assisted intervention* Springer; 2015. p. 234–241.
- 844 Rosenthal SB, Twomey CR, Hartnett AT, Wu HS, Couzin ID. Revealing the hidden networks of interaction in mobile animal groups allows prediction of complex behavioral contagion. *Proceedings of the National Academy of Sciences*. 2015; 112(15):4690–4695.
- 847 Roy AG, Conjeti S, Navab N, Wachinger C. Bayesian QuickNAT: Model Uncertainty in Deep Whole-Brain Segmentation for Structure-wise Quality Control. CoRR. 2018; abs/1811.09800. <http://arxiv.org/abs/1811.09800>.
- 849 Sabour S, Frosst N, Hinton GE. Dynamic routing between capsules. In: *Advances in neural information processing systems*; 2017. p. 3856–3866.
- 851 Saini N, Price E, Tallamraju R, Enficiaud R, Ludwig R, Martinović I, Ahmad A, Black M. Markerless Outdoor Human Motion Capture Using Multiple Autonomous Micro Aerial Vehicles. In: *International Conference on Computer Vision*; 2019. .
- 853 Sandler M, Howard A, Zhu M, Zhmoginov A, Chen LC. Mobilenetv2: Inverted residuals and linear bottlenecks. In: *Proceedings of the IEEE Conference on Computer Vision and Pattern Recognition*; 2018. p. 4510–4520.
- 855 Schiffman R. Drones flying high as new tool for field biologists. American Association for the Advancement of Science; 2014.
- 856 Seethapathi N, Wang S, Saluja R, Blohm G, Kording KP. Movement science needs different pose tracking algorithms. arXiv preprint arXiv:190710226. 2019; .
- 858 Stephens GJ, de Mesquita MB, Ryu WS, Bialek W. Emergence of long timescales and stereotyped behaviors in *Caenorhabditis elegans*. *Proceedings of the National Academy of Sciences*. 2011; 108(18):7286–7289.
- 860 Stowers JR, Hofbauer M, Bastien R, Griessner J, Higgins P, Farooqui S, Fischer RM, Nowikovsky K, Haubensak W, Couzin ID, et al. Virtual reality for freely moving animals. *Nature methods*. 2017; 14(10):995.
- 862 Strandburg-Peshkin A, Farine DR, Couzin ID, Crofoot MC. Shared decision-making drives collective movement in wild baboons. *Science*. 2015; 348(6241):1358–1361.
- 864 Strandburg-Peshkin A, Farine DR, Crofoot MC, Couzin ID. Habitat and social factors shape individual decisions and emergent group structure during baboon collective movement. *Elife*. 2017; 6:e19505.
- 866 Strandburg-Peshkin A, Twomey CR, Bode NW, Kao AB, Katz Y, Ioannou CC, Rosenthal SB, Torney CJ, Wu HS, Levin SA, et al. Visual sensory networks and effective information transfer in animal groups. *Current Biology*. 2013; 23(17):R709–R711.

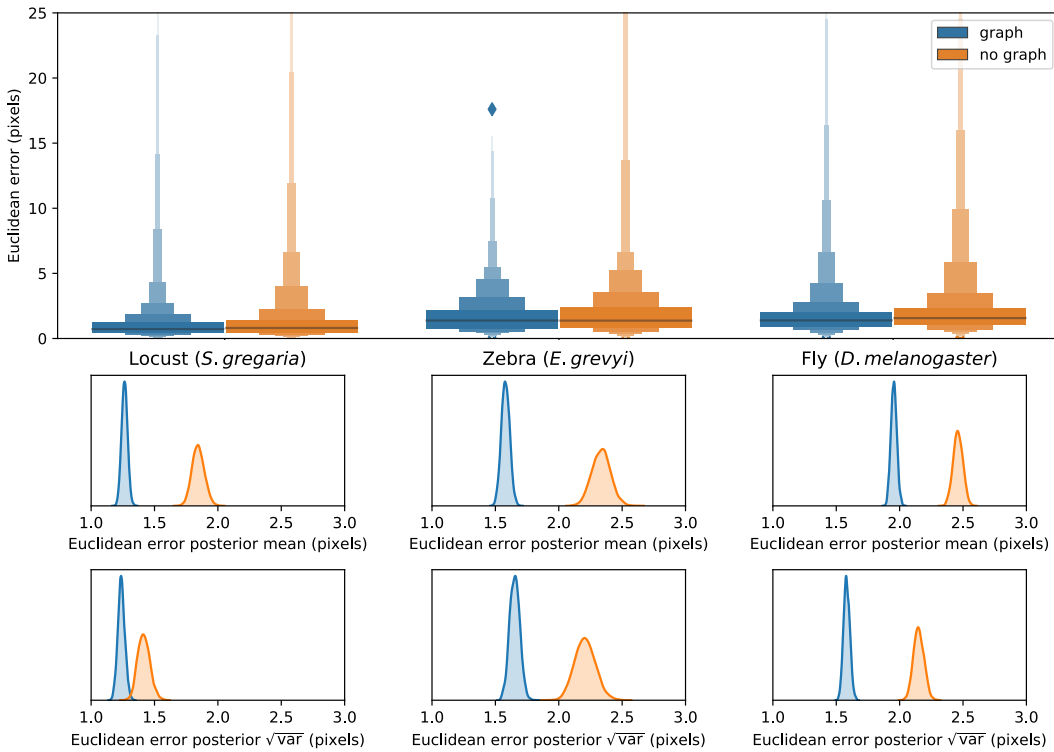
- 868 Todd JG, Kain JS, de Bivort BL. Systematic exploration of unsupervised methods for mapping behavior. *Physical biology*. 2017; 869 14(1):015002.
- 870 Tran D, Hoffman MW, Moore D, Suter C, Vasudevan S, Radul A. Simple, distributed, and accelerated probabilistic programming. 871 In: *Advances in Neural Information Processing Systems*; 2018. p. 7609–7620.
- 872 Uhlmann V, Ramdy P, Delgado-Gonzalo R, Benton R, Unser M. FlyLimbTracker: An active contour based approach for leg 873 segment tracking in unmarked, freely behaving *Drosophila*. *PLoS One*. 2017; 12(4):e0173433.
- 874 Valentin J, Keskin C, Pidlypenskyi P, Makadia A, Sud A, Bouaziz S. TensorFlow Graphics: Computer Graphics Meets Deep 875 Learning. In: ; 2019. .
- 876 Versace E, Caffini M, Werkhoven Z, de Bivort BL. Individual, but not population asymmetries, are modulated by social 877 environment and genotype in *Drosophila melanogaster*. *bioRxiv*. 2019; p. 694901.
- 878 Weigert M, Schmidt U, Boothe T, Müller A, Dibrov A, Jain A, Wilhelm B, Schmidt D, Broaddus C, Culley S, et al. Content-aware 879 image restoration: pushing the limits of fluorescence microscopy. *Nature methods*. 2018; 15(12):1090.
- 880 Werkhoven Z, Rohrsen C, Qin C, Brembs B, de Bivort B. MARGO (Massively Automated Real-time GUI for Object-tracking), a 881 platform for high-throughput ethology. *BioRxiv*. 2019; p. 593046.
- 882 Wild B, Sixt L, Landgraf T. Automatic localization and decoding of honeybee markers using deep convolutional neural networks. 883 CoRR. 2018; abs/1802.04557. <http://arxiv.org/abs/1802.04557>.
- 884 Wiltschko AB, Johnson MJ, Iurilli G, Peterson RE, Katon JM, Pashkovski SL, Abraira VE, Adams RP, Datta SR. Mapping sub-second 885 structure in mouse behavior. *Neuron*. 2015; 88(6):1121–1135.
- 886 Zhang R, Isola P, Efros AA, Shechtman E, Wang O. The unreasonable effectiveness of deep features as a perceptual metric. In: 887 *Proceedings of the IEEE Conference on Computer Vision and Pattern Recognition*; 2018. p. 586–595.
- 888 Zuffi S, Kanazawa A, Berger-Wolf T, Black MJ. Three-D Safari: Learning to Estimate Zebra Pose, Shape, and Texture from Images 889 "In the Wild". In: *International Conference on Computer Vision*; 2019. .
- 890 Zuffi S, Kanazawa A, Jacobs DW, Black MJ. 3D menagerie: Modeling the 3D shape and pose of animals. In: *Proceedings of the 891 IEEE Conference on Computer Vision and Pattern Recognition*; 2017. p. 6365–6373.





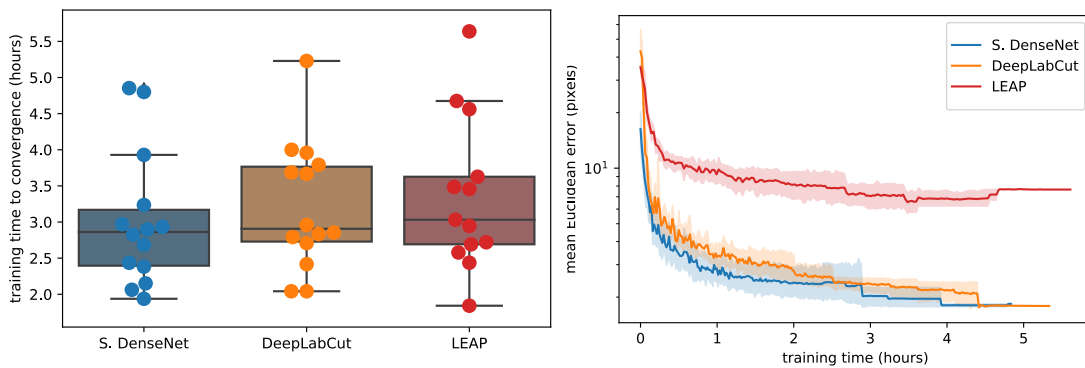
**Appendix 1 Figure 1.** Our subpixel maxima algorithm increases speed without decreasing accuracy. Prediction accuracy on the fly dataset is maintained across downsampling configurations (a). Letter-value plots (a-top) show the raw error distributions for each configuration. Visualizations of the credible intervals (99% highest-density region) of the posterior distributions for the mean and variance (a-bottom) illustrate statistical differences between the error distributions, where using subpixel maxima decreases both the mean and variance of the error distribution. Inference speed is fast and can be run in real-time on single images (batch size = 1) at ~30–110Hz or offline (batch size = 100) upwards of 1000Hz (b). Plots show the inference speeds for our Stacked DenseNet model across downsampling configurations as well as the other models we tested for each of our datasets.

**Figure 1-source data 1.** Raw prediction errors for experiments in Appendix 1 Figure 1a. See "Methods" for details.



**Appendix 1 Figure 2.** Predicting the multi-scale geometry of the posture graph reduces error. Letter-value plots (**top**) show the raw error distributions for each experiment. Visualizations of the posterior distributions for the mean and variance (**bottom**) show statistical differences between the error distributions. Predicting the posture graph decreases both the mean and variance of the error distribution.

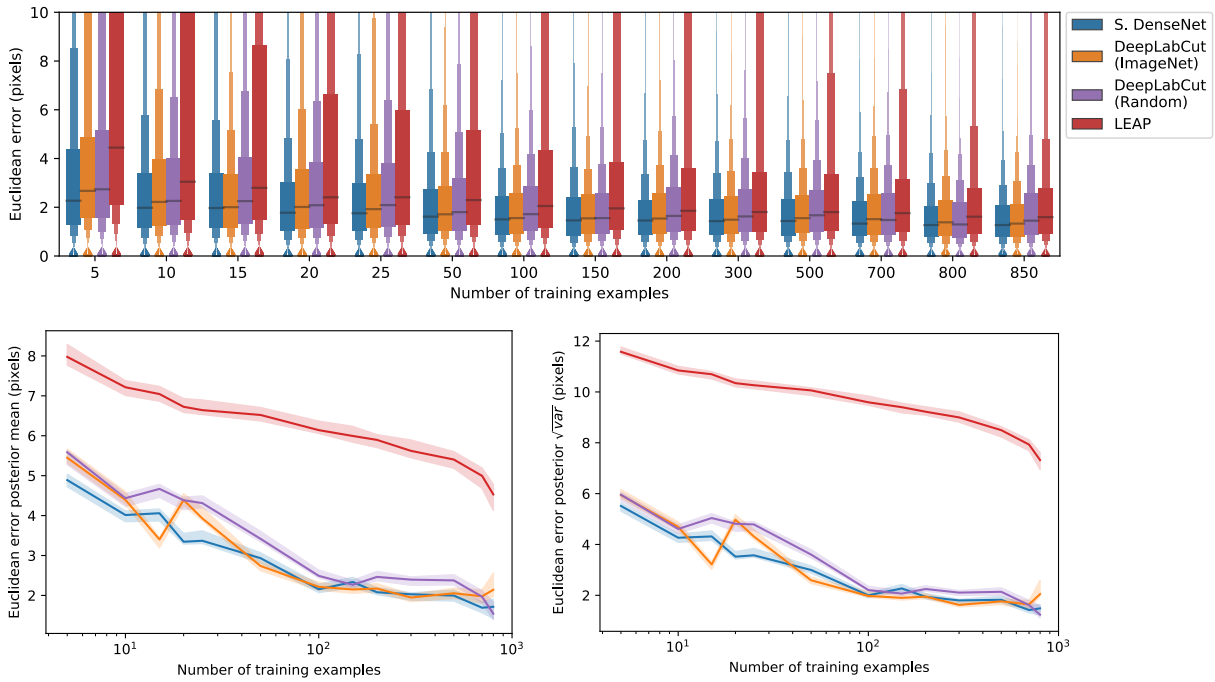
**Figure 2-source data 1.** Raw prediction errors for experiments in Appendix 1 Figure 2. See "Methods" for details.



**Appendix 1 Figure 3.** Training time required for our Stacked DenseNet model, the DeepLabCut model (Mathis et al., 2018), and the LEAP model (Pereira et al., 2019) ( $n=15$  per model) using our zebra dataset. Boxplots and swarm plots (**left**) show the total training time to convergence (<0.001 improvement in validation loss for 50 epochs). Line plots (**right**) illustrate the Euclidean error of the validation set during training, where error bars show bootstrapped ( $n=1000$ ) 99% confidence intervals of the mean. Fully training models to convergence requires only a few hours of optimization (**left**) with reasonable accuracy reached after only 1 hour (**right**) for our Stacked DenseNet model.

**Figure 3-source data 1.** Total training time for each model in Appendix 1 Figure 3.

**Figure 3-source data 2.** Mean euclidean error as a function of training time for each model in Appendix 1 Figure 3.



**Appendix 1 Figure 4.** A comparison of prediction accuracy with different numbers of training examples from our zebra dataset. The error distributions shown as letter-value plots (**top**) illustrate the Euclidean error for the remainder of the dataset not used for training—with a total of 900 labeled examples in the dataset. Line plots (**bottom**) show posterior credible intervals (99% highest-density region) for the mean and variance of the error distributions. We tested our Stacked DenseNet model; the DeepLabCut model (*Mathis et al., 2018*) with transfer learning—i.e., with weights pretrained on ImageNet (*Deng et al., 2009*); the same model without transfer learning—i.e., with randomly-initialized weights; and the LEAP model (*Pereira et al., 2019*). Our Stacked DenseNet model achieves high accuracy using few training examples without the use of transfer learning. Using pretrained weights does slightly decrease overall prediction error for the DeepLabCut model (*Mathis et al., 2018*), but the effect size is relatively small.

**Figure 4-source data 1.** Raw prediction errors for experiments in Appendix 1 Figure 4. See "Methods" for details.

894

895

896

897

898

899

900

901

902

903

904

905

906

907

908

909

910

911

912

913

914

915

916

917

918

919

920

921

922

923

924

925

926

927

928

929

930

931

## Convolutional neural networks (CNNs)

Artificial neural networks like CNNs are complex, non-linear regression models that "learn" a hierarchically-organized set of parameters from real-world data via optimization. These machine learning models are now commonplace in science and industry and have proven to be surprisingly effective for a large number of applications where more conventional statistical models have failed (LeCun et al., 2015). For computer vision tasks, CNN parameters typically take the form of two-dimensional convolutional filters that are optimized to detect spatial features needed to model relationships between high-dimensional image data and some related variable(s) of interest, such as locations in space—e.g., posture keypoints—or semantic labels (Long et al., 2015; Badrinarayanan et al., 2015).

Once a training set is generated (Appendix 3), a CNN model must be selected and optimized to perform the prediction task. CNNs are incredibly flexible with regard to how models are specified and trained, which is both an advantage and a disadvantage. This flexibility means models can be adapted to almost any computer vision task, but it also means the number of possible model architectures and optimization schemes is very large. This can make selecting an architecture and specifying hyperparameters a challenging process. However, most research on pose estimation has converged on a set of models that generally work well for this task (Appendix 4).

After selecting an architecture, the parameters of the model are set to an initial value and then iteratively updated to minimize some objective function, or *loss function*, that describes the difference between the model's predictive distribution and the true distribution of the data—in other words, the likelihood of the model's output is maximized. These parameter updates are performed using a modified version of the gradient descent algorithm (Cauchy 1847) known as *mini-batch stochastic gradient descent*—often referred to as simply *stochastic gradient descent* or *SGD* (Robbins and Monroe, 1951; Kiefer et al., 1952). SGD iteratively optimizes the model parameters using small randomly-selected subsamples, or *batches*, of training data. Using SGD allows the model to be trained on extremely large datasets in an iterative "online" fashion without the need to load the entire dataset into memory. The model parameters are updated with each batch by adjusting the parameter values in a direction that minimizes the error—where one round of training on the full dataset is commonly referred to as an *epoch*. The original SGD algorithm requires careful selection and tuning of hyperparameters to successfully optimize a model, but modern versions of the algorithm, such as *ADAM* (Kingma and Ba, 2014), automatically tune these hyperparameters, which makes optimization more straightforward.

The model parameters are optimized until they reach a convergence criterion, which is some measure of performance that indicates the model has reached a good location in parameter space. The most commonly used convergence criterion is a measure of predictive accuracy—often the loss function used for optimization—on a held-out *validation set*—a subsample of the training data not used for optimization—that evaluates the model's ability to generalize to new "out-of-sample" data. The model is typically evaluated at the end of each training epoch to assess performance on the validation set. Once performance on the validation set stops improving, training is usually stopped to prevent the model from overfitting to the training set—a technique known as *early stopping* (Prechelt, 1998).

933

934

935

936

937

938

939

940

941

942

943

944

945

946

947

948

949

950

951

952

953

954

955

956

957

958

959

960

961

962

963

964

965

966

967

968

## Collecting training data

Depending on the variability of the data, CNNs usually require thousands or tens of thousands of manually-annotated examples in order to reach human-level accuracy. However, in laboratory settings, sources of image variation like lighting and spatial scale can be more easily controlled, which minimizes the number of training examples needed to achieve accurate predictions.

This need for a large training set can be further reduced in a number of ways. Two commonly used methods include (1) *transfer learning*—using a model with parameters that are pre-trained on a larger set of images, such as the ImageNet database (*Deng et al., 2009*), containing diverse features (*Pratt, 1993; Insafutdinov et al., 2016; Mathis et al., 2018*)—and (2) *augmentation*—artificially increasing data variance by applying spatial and noise transformations such as flipping (mirroring), rotating, scaling, and adding different forms of noise or artificial occlusions. Both of these methods act as useful forms of *regularization*—incorporating a prior distribution—that allows the model to generalize well to new data even when the training set is small. Transfer learning incorporates prior information that images from the full dataset should contain statistical features similar to other images of the natural world, while augmentation incorporates prior knowledge that animals are bilaterally symmetric, can vary in their body size, position, and orientation, and that noise and occlusions sometimes occur.

*Pereira et al. (2019)* introduced two especially clever solutions for collecting an adequate training set. First, they cluster unannotated images based on pixel variance and uniformly sample images from each cluster, which reduces correlation between training examples and ensures the training data are representative of the entire distribution of possible images. Second, they use *active learning* where a CNN is trained on a small number of annotated examples and is then used to initialize keypoint locations for a larger set of unannotated data. These pre-initialized data are then manually corrected by the annotator, the model is retrained, and the unannotated data are re-initialized. The annotator applies this process iteratively as the training set grows larger until they are providing only minor adjustments to the pre-initialized data. This “human-in-the-loop”-style annotation expedites the process of generating an adequately large training set by reducing the cognitive load on the annotator—where the pose estimation model serves as a “cognitive partner”. Such a strategy also allows the annotator to automatically select new training examples based on the performance of the current iteration—where low-confidence predictions indicate examples that should be annotated for maximum improvement (Figure 1).

Of course, annotating image data requires software made for this purpose. *Pereira et al. (2019)* provide a custom annotation GUI written in MATLAB specifically designed for annotating posture using an active learning strategy. *Mathis et al. (2018)* recently added a Python-based GUI in an updated version of their software—including active learning and image sampling methods (see *Nath et al. 2019*). Our framework also includes a Python-based GUI for annotating data with similar features to *Mathis et al. (2018)* and *Pereira et al. (2019)*.

970

### Fully-convolutional regression

971

972

973

974

975

976

977

978

979

980

981

982

983

984

985

986

987

988

989

990

991

992

993

For the task of pose estimation, a CNN is optimized to predict the locations of postural keypoints in an image. One approach is to use a CNN to directly predict the numerical value of each keypoint coordinate as an output. However, making predictions in this way removes real-world constraints on the model's predictive distribution by destroying spatial relationships within images, which negates many of the advantages of using CNNs in the first place.

CNNs are particularly good at transforming one image to produce another related image, or set of images, while preserving spatial relationships and allowing for translation-invariant predictions—a configuration known as a *fully-convolutional neural network* or *F-CNN* ([Long et al., 2015](#)). Therefore, instead of directly regressing images to coordinate values, a popular solution ([Newell et al., 2016](#); [Insafutdinov et al., 2016](#); [Mathis et al., 2018](#); [Pereira et al., 2019](#)) is to optimize a F-CNN that transforms images to predict a stack of output images known as *confidence maps*—one for each keypoint. Each confidence map in the output volume contains a single, two-dimensional, symmetric Gaussian indicating the location of each joint, and the scalar value of the peak indicates the confidence score of the prediction—typically a value between 0 and 1. The confidence maps are then processed to produce the coordinates of each keypoint.

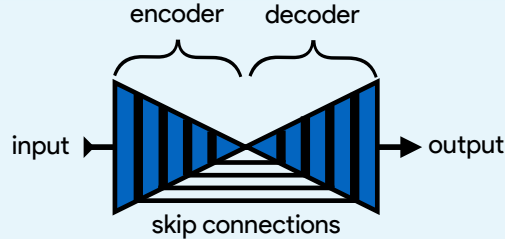
In the case of *multiple pose estimation* where an image contains many individuals, the global geometry of the posture graph is also predicted by training the model to produce *part affinity fields* ([Cao et al., 2017](#))—directional vector fields drawn between joints in the posture graph—or *pairwise terms* ([Insafutdinov et al., 2016](#))—vector fields of the conditional distributions between posture keypoints (e.g.,  $p(\text{foot}|\text{head})$ ). This allows multiple posture graphs to be disentangled from the image using graph partitioning as the vector fields indicate the probability of the connection between joints (see [Cao et al. 2017](#) for details).

994

### Box 1. Encoder-decoder models

995

996  
997



1000

1001

1002

1003

1004

1005

1006

1007

1008

1009

1010

1011

1012

1013

1014

1015

1016

1017

1018

1019

1020

1021

1022

1023

1024

1025

1026

1027

1028

1029

1030

1031

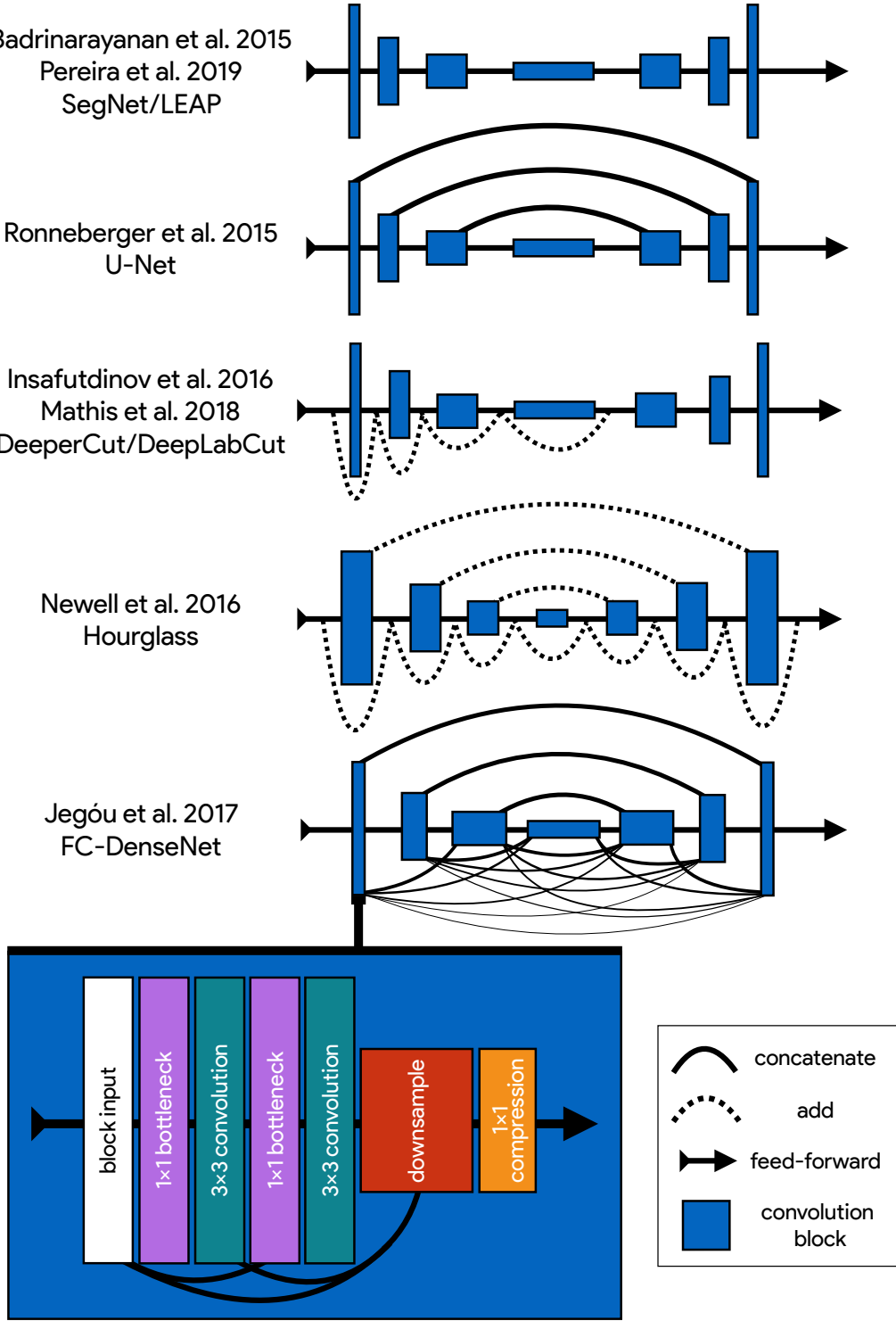
1032

**Box 1 Figure 1.** An illustration of the basic encoder-decoder design. The encoder converts the input images into spatial features, and the decoder transforms spatial features to the desired output.

A popular type of F-CNN (Appendix 4) for solving posture regression problems is known as an *encoder-decoder* model (Figure 1), which first gained popularity for the task of *semantic segmentation*—a supervised computer vision problem where each pixel in an image is classified into one of several labeled categories like “dog”, “tree”, or “road” ([Long et al., 2015](#)). This model is designed to repeatedly convolve and downsample input images in the bottom-up *encoder* step and then convolve and upsample the encoder’s output in the top-down *decoder* step to produce the final output. Repeatedly applying convolutions and non-linear functions, or *activations*, to the input images transforms pixel values into higher-order spatial features, while downsampling and upsampling respectively increases and decreases the scale and complexity of these features.

[Badrinarayanan et al. \(2015\)](#) were the first to popularize a form of this model —known as *SegNet*— for semantic segmentation. However, this basic design is inherently limited because the decoder relies solely on the downsampled output from the encoder, which restricts the features used for predictions to those with the largest spatial scale and highest complexity. For example, a very deep network might learn a complex spatial pattern for predicting “grass” or “trees”, but because it cannot directly access information from the earliest layers of the network, it cannot use the simplest features that plants are green and brown. Subsequent work by [Ronneberger et al. \(2015\)](#) improved on these problems with the addition of *residual* or *skip connections* between the encoder and decoder, where feature maps from encoder layers are concatenated to those decoder layers with the same spatial scale. This set of connections then allows the optimizer, rather than the user, to select the most relevant spatial scale(s) for making predictions.

[Jégou et al. \(2017\)](#) are the latest to advance the encoder-decoder paradigm. These researchers introduced a fully-convolutional version of [Huang et al.’s \(2017a\)](#) *DenseNet* architecture known as a *fully-convolutional DenseNet*, or *FC-DenseNet*. FC-DenseNet’s key improvement is an elaborate set of feed-forward residual connections where the input to each convolutional layer is a concatenated stack of feature maps from all previous layers. This densely-connected design was motivated by the insight that many state-of-the-art models learn a large proportion of redundant features. Most CNNs are not designed so that the final output layers can access all feature maps in the network simultaneously, and this limitation causes these networks to “forget” and “relearn” important features as the input images are transformed to produce the output. In the case of the incredibly popular ResNet-101 ([He et al., 2016](#)) nearly 40% of the features can be classified as redundant ([Ayinde and Zurada, 2018](#)). A densely-connected architecture has the advantages of reduced feature redundancy, increased feature reuse, enhanced feature propagation from early layers to later layers, and subsequently, a substantial reduction in the number of parameters needed to achieve state-of-the-art results ([Huang et al., 2017a](#)). Recent work has also shown that DenseNet’s elaborate residual connections have the pleasant side-effect of convexifying the loss landscape during optimization ([Li et al., 2018](#)), which allows for faster optimization and increases the likelihood of reaching a good optimum.



**Appendix 4 Figure 1.** An illustration showing the progression of encoder-decoder architectures from the literature—ordered by performance from top to bottom (see Appendix 4 Box 1 for further details). Most advances in performance have come from adding connections between layers in the network, culminating in FC-DenseNet from Jégou et al. (2017). Lines in each illustration indicate connections between convolutional blocks with the thickness of the line indicating the magnitude of information flow between layers in the network. The size of each convolution block indicates the relative number of feature maps (width) and spatial scale (height). The callout for FC-DenseNet (Jégou et al. 2017; **bottom-left**) shows the elaborate set of skip connections within each densely-connected convolutional block as well as our additions of bottleneck and compression layers (described by Huang et al. 2017a) to increase efficiency (Appendix 8)

1034  
1035  
1036  
1037  
1038  
1039  
1040  
1041  
1042  
1043  
1044  
1045  
1046  
1047  
1048  
1049**The state of the art for individual pose estimation**

Many of the current state-of-the-art models for individual posture estimation are based on the design from [Newell et al. \(2016\)](#) (e.g., [Ke et al. 2018](#), [Chen et al. 2017](#); also see benchmark results from [Andriluka et al. 2014](#)), but employ various modifications that increase complexity to improve performance. [Newell et al. \(2016\)](#) employ what they call a *Stacked Hourglass* network (Appendix 4 Figure 1), which consists of a series of multi-scale encoder-decoder *hourglass* modules connected together in a feed-forward configuration (Figure 2). The main novelties these researchers introduce include (1) stacking multiple hourglass networks together for repeated top-down-bottom-up inference, (2) using convolutional blocks based on the ResNet architecture ([He et al., 2016](#)) with residual connections between the input and output of each block, and (3) using residual connections between the encoder and decoder (similar to [Ronneberger et al. 2015](#)) with residual blocks in between. [Newell et al. \(2016\)](#) also apply a technique known as *intermediate supervision* (Figure 2) where the loss function used for model training is applied to the output of each hourglass as a way of improving optimization across the model's many layers. Recent work by [Jégou et al. \(2017\)](#) has further improved on this encoder-decoder design (see Appendix 4 Box 1 and Appendix 4 Figure 1), but to the best of our knowledge, the model introduced by [Jégou et al. \(2017\)](#) has not been previously applied to pose estimation.

1050      **Appendix 6**

1051

1052

1053

1054

1055

1056

1057

1058

1059

1060

1061

1062

1063

1064

1065

1066

1067

### Overparameterization and the limitations of LEAP

Overparameterization is a key limitation for many pose estimation methods, and addressing this problem is critical for high-performance applications. *Pereira et al. (2019)* approached this problem by designing their LEAP model after the model from *Badrinarayanan et al. (2015)*, which is a straightforward encoder-decoder design (Appendix 4 Figure 1; Appendix 4 Box 1). They benchmarked their model on posture estimation tasks for laboratory animals and compared performance with the more-complex Stacked Hourglass model from *Newell et al. (2016)*. They found their smaller, simplified model achieved equal or better median accuracy with dramatic improvements in inference speed up to 185 Hz. However, *Pereira et al. (2019)* first rotationally and translationally aligned each image to improve performance, and their reported inference speeds do not include this computationally expensive preprocessing step. Additionally, rotationally and translationally aligning images is not always possible when the background is complex or highly-variable—such as in field settings—or the study animal has a non-rigid body. This limitation makes the LEAP model (*Pereira et al., 2019*) unsuitable in many cases. While their approach is simple and effective for a multitude of experimental setups, the LEAP model (*Pereira et al., 2019*) is also implicitly limited in the same ways as *Badrinarayanan et al.*'s SegNet model (see Appendix 4 Box 1 for details). The LEAP model cannot make predictions using multiple spatial scales and is not robust to data variance such as rotations (*Pereira et al., 2019*).

1069  
1070  
1071  
1072  
1073  
1074  
1075  
1076  
1077  
1078  
1079  
1080

### Linear model fitting with Stan

We estimated the joint posterior  $p(\theta_\mu, \theta_\phi | X, y)$  for each model using the No-U-Turn Sampler (NUTS; *Hoffman and Gelman 2014*), a self-tuning variant of the Hamiltonian Monte Carlo (HMC) algorithm (*Duane et al., 1987*), implemented in Stan (*Carpenter et al., 2017*). We drew HMC samples using 4 independent Markov chains consisting of 1,000 warm-up iterations and 1,000 sampling iterations for a total of 4,000 sampling iterations. To speed up sampling, we randomly subsampled 20% of the data from each replicate when fitting each linear model, and we fit each model 5 times to ensure the results were consistent. All models converged without any signs of pathological behavior. We performed a posterior predictive check by visually inspecting predictive samples to assess model fit. For our priors we chose relatively uninformative distributions  $\theta_\mu \sim \text{Cauchy}(0, 5)$  and  $\theta_\phi \sim \text{Cauchy}(0, 10)$ , but we found that the choice of prior generally did not have an effect on the final result due to the large amount of data used to fit each model.

1082  
1083 **Stacked DenseNet**  
1084

1085 Our Stacked DenseNet model consists of an initial  $7 \times 7$  convolutional layer with stride 2, to efficiently  
 1086 downsample the input resolution—following [Newell et al. \(2016\)](#)—followed by a stack of densely-  
 1087 connected hourglass networks with intermediate supervision (Appendix 5) applied at the output of  
 1088 each network. We also include hyperparameters for the bottleneck and compression layers described  
 1089 by [Huang et al. \(2017a\)](#) to make the model as efficient as possible. These consist of applying a  $1 \times 1$   
 convolution to inexpensively compress the number of feature maps before each  $3 \times 3$  convolution as well  
 as when downsampling and upsampling (see [Huang et al. 2017a](#) and Appendix 4 Figure 1 for details).

1090  
1091 **Model hyperparameters**  
1092

1093 For our Stacked Hourglass model we used a block size of 64 filters (64 filters per  $3 \times 3$  convolution) with a  
 1094 bottleneck factor of 2 ( $64/2 = 32$  filters per  $1 \times 1$  bottleneck block). For our Stacked DenseNet model we  
 1095 used a growth rate of 48 (48 filters per  $3 \times 3$  convolution), a bottleneck factor of 1 ( $1 \times$  growth rate = 48  
 1096 filters per  $1 \times 1$  bottleneck block), and a compression factor of 0.5 (feature maps compressed with  $1 \times 1$   
 1097 convolution to  $0.5m$  when upsampling and downsampling, where  $m$  is the number of feature maps). For  
 1098 our Stacked DenseNet model we also replaced the typical configuration of batch normalization and ReLU  
 1099 activations ([Goodfellow et al., 2016](#)) with the more recently-developed self-normalizing SELU activation  
 1100 function ([Klambauer et al., 2017](#)), as we found this modification increased inference speed. For the  
 1101 LEAP model ([Pereira et al., 2019](#)) we used a  $1 \times$  resolution output with integer-based global maxima  
 1102 because we wanted to compare our more complex models with this model in the original configuration  
 1103 described by [Pereira et al. \(2019\)](#). The LEAP model could be modified to output smaller confidence  
 1104 maps and increase inference speed, but because there is no obvious "best" way to alter the model to  
 1105 achieve this, we forgo any modification. Additionally, applying our subpixel maxima algorithm at high  
 resolution reduces inference speed compared to integer-based maxima, so this would bias our speed  
 comparisons.

1106  
1107 **Our implementation of the DeepLabCut model**  
1108

1109 Because the DeepLabCut model from [Mathis et al. \(2018\)](#) was not implemented in Keras (a requirement  
 1110 for our pose estimation framework), we re-implemented it. Implementing this model directly in our  
 1111 framework is important to ensure model training and data augmentation are identical when making  
 1112 comparisons between models. As a consequence, our version of this model does not exactly match the  
 1113 description in the paper but is identical except for the output. Rather than using the location refinement  
 1114 maps described by [Insafutdinov et al. \(2016\)](#) and post-processing confidence maps on the CPU, our  
 1115 version of the DeepLabCut model ([Mathis et al., 2018](#)) has an additional transposed convolutional layer  
 1116 to upsample the output to  $\frac{1}{4} \times$  resolution and uses our subpixel maxima algorithm.

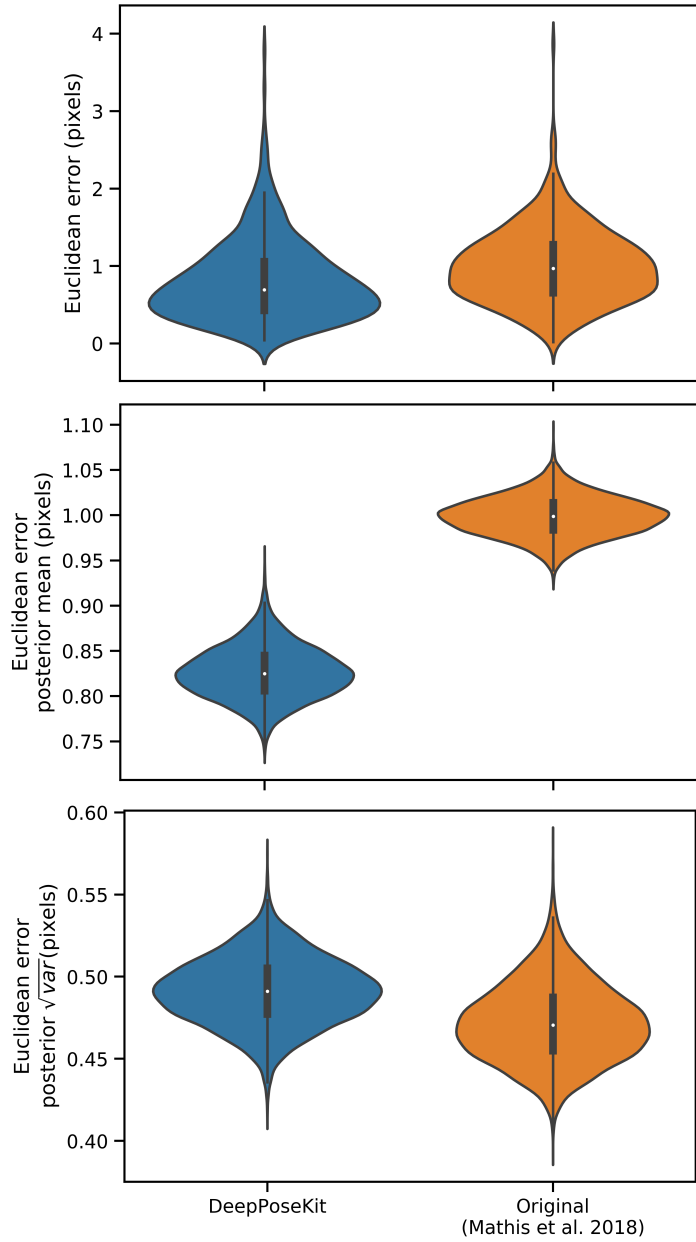
1117 To demonstrate that our implementation of the DeepLabCut model matches the performance  
 1118 described by [Mathis et al. \(2018\)](#), we compared prediction accuracy between the two frameworks using  
 1119 the odor-trail mouse dataset provided by [Mathis et al. \(2018\)](#) (downloaded from <https://github.com/AlexEMG/DeepLabCut/>). This dataset consists of 116 images of a freely-moving individual mouse labeled  
 1120 with four keypoints describing the location of the snout, ears, and the base of the tail. See [Mathis et al. \(2018\)](#)  
 1121 for further details on this dataset. We trained both models using 95% training and 5%  
 1122 validation data and applied data augmentations for both frameworks using the data augmentation  
 1123 procedure described by [Nath et al. \(2019\)](#). We tried to match these data augmentations as best as  
 1124 possible in DeepPoseKit; however, rather than cropping images as described by [Nath et al. \(2019\)](#), we  
 1125 randomly translated the images independently along the horizontal and vertical axis by drawing from a  
 1126 uniform distribution in the range [-100%, +100%]—where percentages are relative to the size of each  
 axis. Translating the images in this way should serve the same purpose as cropping them.

1127 We trained the original DeepLabCut model ([Mathis et al., 2018](#)) using the default settings and  
 1128 recommendations from [Nath et al. \(2019\)](#) for 1 million training iterations. See [Mathis et al. \(2018\)](#);  
 1129 [Nath et al. \(2019\)](#) for further details on the data augmentation and training routine for the original  
 1130 implementation of the DeepLabCut model ([Mathis et al., 2018](#)). For our re-implementation of the  
 1131 DeepLabCut model ([Mathis et al., 2018](#)) we trained the model with the same batch size and optimization  
 1132 scheme described in the "Model training" section. We then calculated the prediction accuracy on the

1128  
1129  
1130  
1131  
1132  
1133  
1134  
1135  
1136  
1137  
1138  
1139  
1140  
1141  
1142  
1143  
1144  
1145  
1146  
1147  
1148  
1149  
1150  
1151

full data set. We repeated this procedure five times for each model and fit a Bayesian linear model to a randomly selected subset of the evaluation data to compare the results statistically (see Appendix 7).

These results demonstrate that our re-implementation of and modification to the DeepLabCut model (*Mathis et al., 2018*) have little effect on prediction accuracy (Appendix 8 Figure 1). We also provide qualitative comparisons of these results in Appendix 8 Figure 1-Figure supplement 1 and Appendix 8 Figure 1-video 1. For these qualitative comparisons, we also added an additional rotational augmentation (drawing from a uniform distribution in the range [-180°, +180°]) when training our implementation of the DeepLabCut model (*Mathis et al., 2018*) as we noticed this improved generalization to the video for situations where the mouse rotated its body axis. To the best of our knowledge, rotational augmentations are not currently available when using the software from *Mathis et al. (2018); Nath et al. (2019)*, which demonstrates the flexibility of the data augmentation pipeline (*Jung, 2018*) for DeepPoseKit. The inference speed for the odor-trail mouse dataset using our implementation of the DeepLabCut model (*Mathis et al., 2018*) is ~49Hz with a batch size of 64 (offline speeds) and ~35Hz with a batch size of 1 (real-time speeds) at full resolution 640x480, which matches well with results from *Mathis and Warren (2018)* of ~47Hz and ~32Hz respectively. This suggests our modifications did not affect the speed of the model and that our speed comparisons are also reasonable. Because the training routine could be changed for any underlying model—including the new models we present in this paper—this factor is not relevant when making comparisons as long as training is identical for all models being compared, which we ensure when performing our comparisons.



**Appendix 8 Figure 1.** Prediction errors for the odor-trail mouse dataset from [Mathis et al. \(2018\)](#) using the original implementation of the DeepLabCut model ([Mathis et al., 2018; Nath et al., 2019](#)) and our modified version of this model implemented in DeepPoseKit. Mean prediction error is slightly lower for the DeepPoseKit implementation, but there is no discernible difference in variance. These results indicate that the models achieve nearly identical prediction accuracy despite modification. We also provide qualitative comparisons of these results in Appendix 8 Figure 1-Figure supplements 1 and 2, and Appendix 8 Figure 1-video 1.

**Figure 1-Figure supplement 1.** Plots of the predicted output for Appendix 8 Figure 1-video 1 comparing our implementation of the DeepLabCut model ([Mathis et al., 2018](#)) in DeepPoseKit vs. the original implementation from [Mathis et al. \(2018\); Nath et al. \(2019\)](#). Note the many fast jumps in position for the original verison from [Mathis et al. \(2018\)](#), which indicates prediction errors.

**Figure 1-Figure supplement 2.** Plots of the temporal derivatives of the predicted output for Appendix 8 Figure 1-video 1 comparing our implementation of the DeepLabCut model ([Mathis et al., 2018](#)) in DeepPoseKit vs. the original implementation from [Mathis et al. \(2018\); Nath et al. \(2019\)](#). Note the many fast jumps in position for the original verison from [Mathis et al. \(2018\)](#), which indicates prediction errors.

**Figure 1-video 1.** A video comparison of the tracking output of the DeepLabCut model ([Mathis et al., 2018](#)) reimplemented in DeepPoseKit vs. the original implementation from [Mathis et al. \(2018\); Nath et al. \(2019\)](#). <https://youtu.be/YFmO5C0hUw4>

**Figure 1-source data 1.** Raw prediction errors for our DeepLabCut model ([Mathis et al., 2018](#)) reimplemented in DeepPoseKit in Appendix 8 Figure 1. See "Methods" for details.

**Figure 1-source data 2.** Raw prediction errors for the original DeepLabCut model from [Mathis et al. \(2018\)](#) in Appendix 8 Figure 1. See "Methods" for details.

1153

1154

1155

1156

1157

1158

1159

1160

1161

1162

1163

1164

1165

### Depthwise-separable convolutions for memory-limited applications

In an effort to maximize model efficiency, we also experimented with replacing 3x3 convolutions in our model implementations with 3x3 depthwise-separable convolutions —first introduced by [Chollet \(2017\)](#) and now commonly used in fast, efficient “mobile” CNNs (e.g., [Sandler et al. 2018](#)). In theory this modification should both reduce the memory footprint of the model and increase inference speed. However we found that, while this does drastically decrease the memory footprint of our already memory-efficient models, it slightly decreases accuracy and does not improve inference speed, so we opt for a full 3x3 convolution instead. We suspect that this discrepancy between theory and application is due to inefficient implementations of depthwise-separable convolutions in many popular deep learning frameworks, which will hopefully improve in the near future. At the moment we include this option as a hyperparameter for our Stacked DenseNet model, but we recommend using depthwise-separable convolutions only for applications that require a small memory footprint such as training on a lower-end GPU with limited memory or running inference on a mobile device.

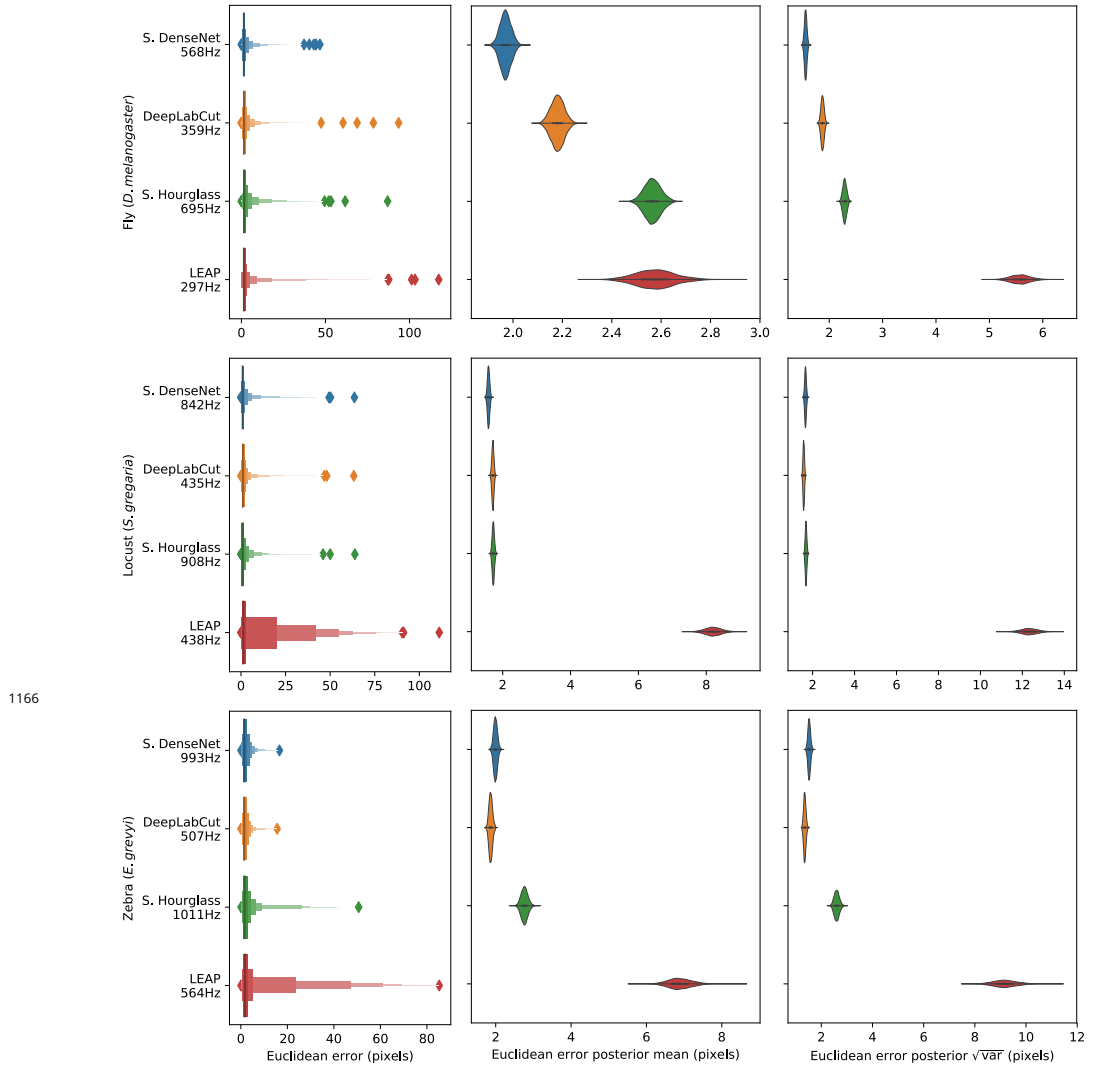


**Figure 3-Figure supplement 1.** Euclidean error distributions for each model across our three datasets. Letter-value plots (**left**) show the raw error distributions for each model. Violinplots of the posterior distributions for the mean and variance (**right**) show statistical differences between the error distributions. Overall the LEAP model ([Pereira et al., 2019](#)) was the worst performer on every dataset in terms of both mean and variance. Our Stacked Densenet model was the best performer for the fly dataset, while our Stacked DenseNet model and the DeepLabCut model ([Mathis et al., 2018](#)) both performed equally well on the locust and zebra datasets. The posteriors for the DeepLabCut model ([Mathis et al., 2018](#)) and our Stacked DenseNet model are highly overlapping for these datasets, which suggests they are not statistically discernible from one another. Our Stacked Hourglass model ([Newell et al., 2016](#)) performed equally to the DeepLabCut model ([Mathis et al., 2018](#)) and our Stacked DenseNet model for the locust dataset but performed slightly worse for the fly and zebra datasets.

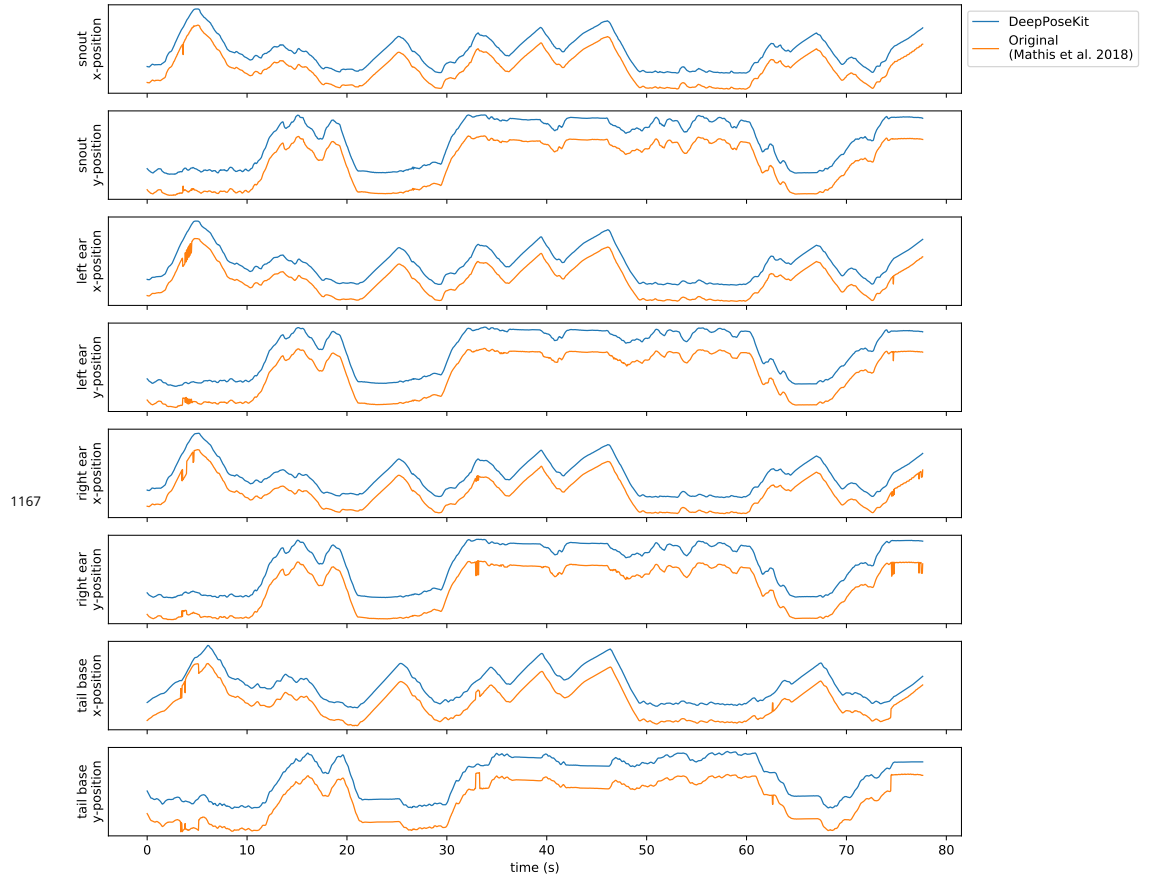


**Figure 1-Figure supplement 1.** Plots of the predicted output for Appendix 8 Figure 1-video 1 comparing our implementation of the DeepLabCut model (*Mathis et al., 2018*) in DeepPoseKit vs. the original implementation from *Mathis et al. (2018); Nath et al. (2019)*. Note the many fast jumps in position for the original verison from *Mathis et al. (2018)*, which indicates prediction errors.

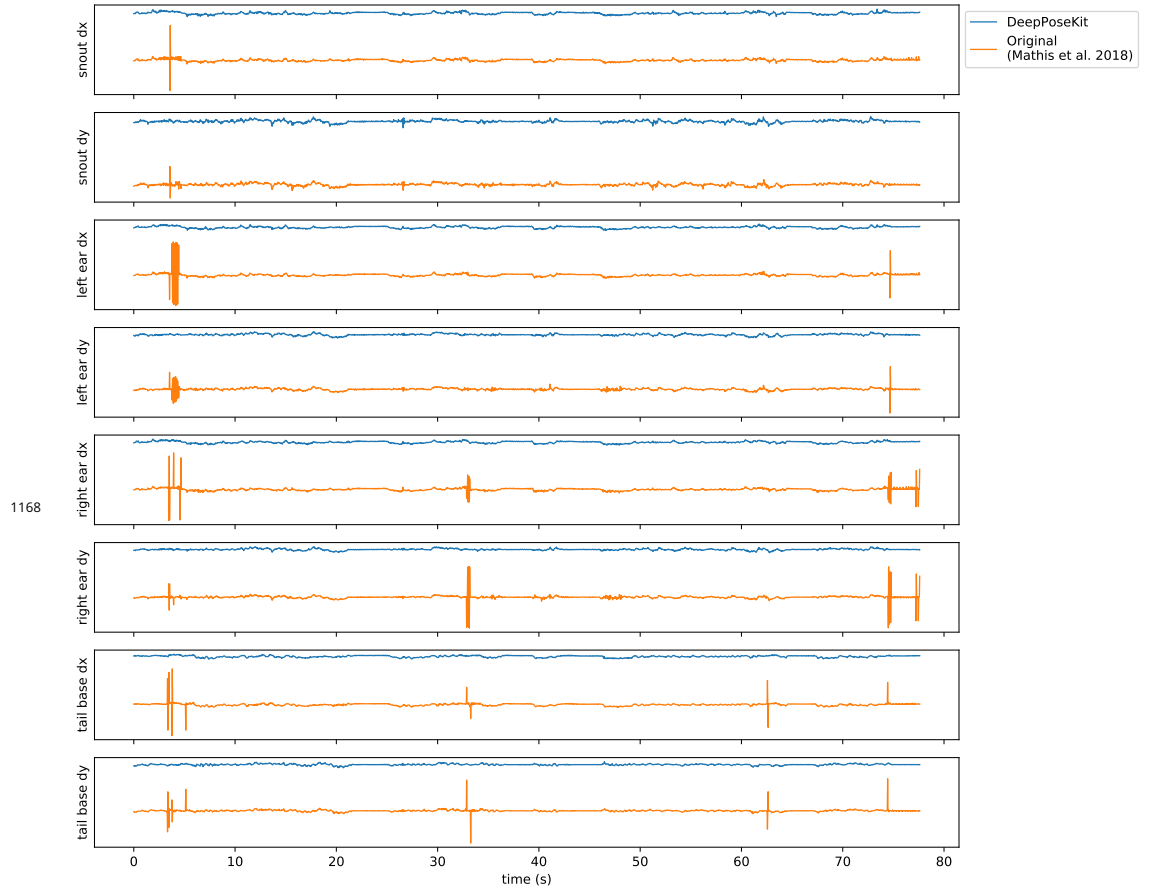


**Figure 1-Figure supplement 2.** Plots of the temporal derivatives of the predicted output for Appendix 8 Figure 1-video 1 comparing our implementation of the DeepLabCut model (*Mathis et al., 2018*) in DeepPoseKit vs. the original implementation from *Mathis et al. (2018); Nath et al. (2019)*. Note the many fast jumps in position for the original verison from *Mathis et al. (2018)*, which indicates prediction errors.